



Master of Science in Informatics at Grenoble
Master Mathématiques Informatique - spécialité Informatique
option Graphics, Vision and Robotics

3D Doppler Ultrasound Image Analysis for Brain Shift Compensation

J.M.N.C. Jayalath

2013-06-20

Research project performed at TIMC-IMAG

Under the supervision of:
Prof. Yohan Payan, TIMC-IMAG
Dr. Marek Bucki, TIMC-IMAG

Defended before a jury composed of:
Prof. Rémi Ronfard
Prof. James Crowley
Prof. Marie-Christine Fauvet
Prof. Fabrice Jaillet

June

2013

Abstract

Image guided surgery has become a common practice in modern day neurosurgery where surgeons rely on computer assistance and image guidance to perceive topological and locational information about the patient's brain. These systems typically use the preoperative MRI images of the patient acquired before the surgery. However, significant errors might be introduced into the surgical navigation through intraoperative brain deformations, known as brain-shift. Intraoperative Doppler ultrasound imaging of brain vascular data has shown promising results to compensate for this error by registering intraoperative Doppler Ultrasound vascular data with preoperative Magnetic Resonance Angiography vascular data.

This report first discusses a 3D reconstruction technique to reconstruct the Doppler Ultrasound vascular tree from 2D Doppler Ultrasound images. The results are accurate and have been tested with physical phantom data.

The centerlines of both preoperative and intraoperative vascular data are extracted as registration data. The centerline representation completely captures the topological and geometrical properties of 3D vascular data and their compact representation dramatically increases the computational time during registration. However, the centerlines contain 5-10% outliers, which lead to miss registrations. To overcome this, a 3D image-pruning algorithm is developed and tested on different 3D images. The test results show this noise removal process can significantly enhance the registration accuracy.

The techniques developed are evaluated on a digital phantom where the Doppler images and brain shift is simulated. Extensive evaluation is carried out simulating brain shift of different displacements ranging from 5mm to 40mm. The target registration error is less than 1.5mm for almost 80% of the registrations with 30-40mm displacements.

However, these evaluations should be carried out on a new physical phantom data or clinical data to further improve the techniques and to capture the actual physical phenomena.

Acknowledgements

I should first thank my Mom for being such a wonderful woman after my Dad unfortunately passed away during my Advanced Level studies. My parents first noticed my interest and abilities in Science and Engineering and always encouraged and gave me all the support to realize my higher studies. Coming from a rural place of Sri Lanka, I could have never carried out a research degree in one of the best Universities in France if it was not for my parents. Thank you again Mom, Dad and Sister.

I should be very thankful to Dr. Yohan Payan and Dr. Marek Bucki for recruiting me to work as a Research Engineer in TIMC-IMAG before I started my Master2 with MoSIG Program. They directed me to the Master2 course and gave me all the support and advice starting from application to the acceptance. The support they gave me during the Master Thesis project really helped me to grow as a research student. They both were such an influence on my work and it will definitely carry with me through my career. Both of them supported me throughout my stay at Grenoble, professionally and personally, and I will never forget that support.

I really appreciate Dr. James Crowley's support and advise during my application to MoSIG program and suggesting me to apply for the available scholarships.

I was very lucky to be awarded Grenoble INP Excellence award for studies with MoSIG Program and it helped me to focus on my studies without financial obstacles. Thank you very much Granoble INP Foundation.

In my personal circle, I would like to thank Prasad Samarakoon for reviewing my final report and gave very important feedbacks.

I thank all the Professors of the MoSIG course for providing us with a well-structured and well-balanced course.

I appreciate the support given by the students and researchers of TIMC-IMAG during my Master Thesis project.

Table of Contents

1.	Introduction	1
1.1	Brain Shift Compensation and Techniques	2
1.2	Research Objective.....	3
1.3	GMCAO System and Limitations	4
1.3.1	Pre-Operative Phase	4
1.3.2	Intra-Operative Phase.....	4
1.3.3	Limitations of the System	4
1.4	State of the Art of Doppler Ultrasound in Brain Shift	5
2.	Methodology	6
3.	Doppler Ultrasound Reconstruction.....	7
3.1	3D Ultrasound reconstruction	7
3.1.1	Methods of 3D ultrasound imaging.....	7
3.2	Power Doppler Acquisition.....	8
3.2.1	US image geometry	8
3.2.2.	Individual US image preprocessing	9
3.3	3D Reconstruction of Doppler Vascular Tree.....	9
3.3.1	Image Data and Coordinate Systems	9
3.4.2	Mapping Physical Point to US Image Data.....	10
3.3.3	Interpolating image data.....	12
3.4	Reconstruction of Synthetic Data.....	13
3.4.1	Synthetic US Generation.....	13
3.4.2.	Interpolation artifacts in Synthetic Data.....	13
3.6	3D reconstruction of phantom data	15
3.6.1	Building the Phantom.....	15
3.6.2.	Reconstruction results and evaluation.....	15
4.	Vessel Topological Skeleton Extraction	17
4.1	Topological Skeleton of Geometric Shapes	17
4.1.1	Skeletonization by Thinning	18
4.1.2	ITK implementation of the Thinning algorithm.....	19
4.2	Results of the Image Thinning	19

5.	Elastic/Nonlinear Image Registration	21
5.1	Registration Workflow.....	21
5.2	Elastic Registration	21
5.2.1	Registration Overview.....	21
5.2.2	Energy Minimization.....	23
5.2.3	Grid Subdivision	23
5.3	Qualitative Analysis of the Algorithm	24
6.	Registration Filtering and Enhancement	25
6.1	Curve Skeleton Pruning	25
6.1.1	Digital Topology	25
6.1.2	Pruning Workflow.....	26
6.1.3	First Level Curve Skeleton Classification.....	27
6.1.4	Noise Removal/Pruning	28
6.1.5.	Classify Junction Clusters Completely	30
6.1.6	Vascular Tree Labeling	32
6.1.7	Centeredness of Thinning Algorithm	34
7.	Synthetic Data Generation and Synthetic Brain Shift	35
7.1	Qualitative properties of actual Doppler US	35
7.2	Digital Phantom.....	35
8.	Evaluation and Discussion	37
8.1	Evaluation Platform.....	37
8.2	Results	39
8.3	Discussion	41
9.	Conclusion.....	42
	References:	44

1. Introduction

Image guided surgery [1], was investigated in 80s with stereotactic neurosurgery procedures where it provided the means to introduce probes into the brain at precisely defined locations with the use of attached frame based coordinate system in patient's head. The technology has since evolved to an extent where even robotic surgeries are performed using tele-operative platforms.

Early systems used stereotactic frames to define the coordinate systems of the physical patient and used this coordination knowledge to define precise surgical site locations. However, with the advent of truly three dimensional images, first Computed Tomography (CT) and then Magnetic Resonance Imaging (MRI), the systems evolved rapidly using the volumetric images with the stereotactic frames to guide and investigate the surgery in real time giving the image feedback to the surgeon [2-4]. This is known as Image Guided Surgery (IGS) or Computer Assisted Surgery (CAS).

The early adoption of the IGS systems was in the field of neurosurgery. Surgeons were convinced that the brain is confined in the skull allowing rigid image to physical patient registration, which would be used to plan and perform surgery. However, this registration was found to be compromised by the phenomena, now called "Brain Shift" [6]. Brain Shift is nonlinear deformation of the brain tissues that occur in the course of surgery because of physical (dura opening, gravity, loss of cerebra-spinal fluid, actions of the neurosurgeon, etc.) and physiological phenomena (swelling due to osmotic drugs, anesthetics, etc.), and some of them still being not completely known (Figure 1.1).

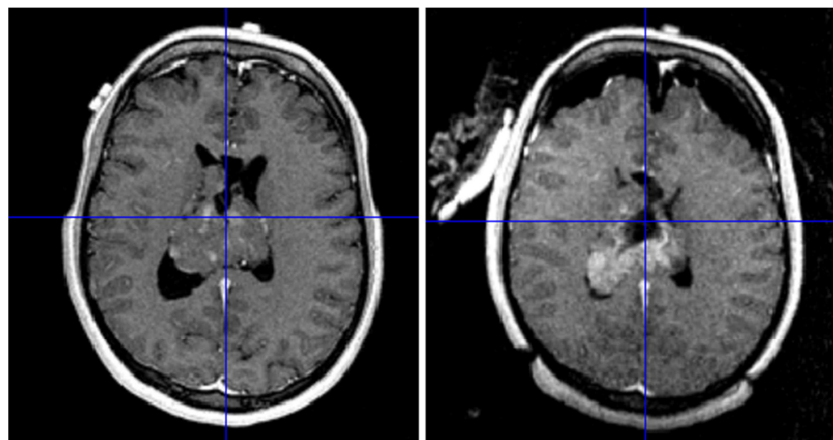


Figure 1-1: Pre and Intraoperative MRI showing the effect brain shift

Because of the brain-shift, pre-operative images no longer exhibit registered correspondence between physical and image spaces and pre-operative based neuro-navigation is therefore strongly compromised by intra-operative brain deformation. In [7], the researchers observed a great variability of the brain-shift ranging up to 24 mm for cortical displacement and exceeding 3

mm for the deep tumor margin; the authors claim non-correlation of the brain surface and the deeper structures. The dynamic brain shift process evolves differently in distinct brain regions, with a surface shift that occurs throughout surgery [8] (the authors attribute that to gravity) and with a subsurface shift that mainly occurs during resection (that the authors attribute to the collapse of the resection cavity and to the intra-parenchymal changes).

1.1 Brain Shift Compensation and Techniques

The evident solution to this problem is updating or replacing the pre-operative images to exhibit the changes during the surgery in the patient's brain tissues, which would guarantee the correct mapping from physical space again.

Extensive work has been carried out in literature to compensate for brain shift using intra-operative imaging modalities: CT, MRI and Ultrasound. Early work suggested the construction and usage of an operating suite outfitted with an intra-operative CT scanner [10-11]. CT scans, acquired before, during and after the surgery, were used to guide and evaluate the surgery. Using MRI as an intra-operative image modality has long been studied [13-17] and current research in this direction is carried out both in academia and industry. Intra-operative MRI is available, although it is not in widespread use, mostly due to the requirement for specialized interventional suites and the cost incurred.

Intra-operative B-mode Ultrasound has been studied to replace the high cost complex CT and MRI intra-operative imaging either alone [18-19] or in conjunction with per-operative MRI [20-21]. Overlaying of 2D ultrasound images on preoperative MR images to understand the correspondence between preoperative and intra-operative images to estimate the Brain-shift was studied in [19], this method is adopted in some commercially available systems [20-22], and much research is still carried out to find the correspondence between multi modalities. However, MRI-Ultrasound (US) image fusion is still not mature enough to capture brain shift very accurately [21].

An interesting work has been done in [31-32] to use Doppler ultrasound as an intra-operative imaging modality to compensate for brain-shift. The Doppler ultrasound is a very interesting modality, which can be used to image blood vessels inside the brain. It has been seen that during brain-shift, the vascular tree of the brain move similar to the tissues and the vascular tree can be used to identify the brain-shift [31-32].

In addition, stereoscopic cameras and laser range scanners [26] are being used to scan the surgical site surface and perform surface to surface registration to understand the brain-shift. However, major problem of using surface based techniques is that the accuracy is highly compromised by how much surface is exposed. In addition, it cannot be guaranteed that, the shift is the same in the inner region of the brain to that of the surface.

Recent research has shown a great promise of using Biomechanical Models [25] [27] together with intra-operative ultrasound Doppler image, stereoscopic camera image or laser range image information to compensate the brain-shift. Therefore, biomechanical models, together with intra-operative images, play a crucial role in a hybrid solution.

1.2 Research Objective

Blood vessels are important and useful features inside the brain mainly because they are distributed well inside the brain and can be imaged using techniques such as Magnetic Resonance Angiography (MRA), Power Doppler ultrasound and Fluorescence imaging. Therefore, brain vessels are an interesting candidate for brain shift compensation using image feature registration of preoperative and intraoperative image data. The studies [31-33] have shown promising results for compensating for brain shift using Doppler ultrasound images. The group GMCAO (Gestes Médico-Chirurgicaux Assistés par Ordinateur) at TIMC-IMAG has taken a different direction (Figure 1-2) to tackle the problem of brain-shift [25] [31] using biomechanical modeling with Doppler intra-operative imaging and has shown great promise with the initial work.

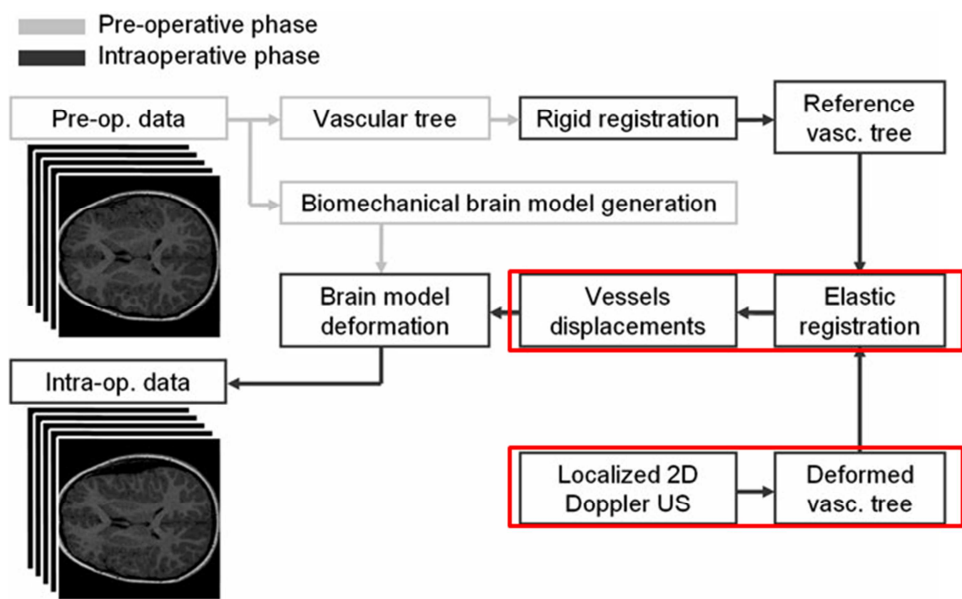


Figure 1-2: System Overview, Neuro Navigator supporting brain shift [GMCAO]

Source: [31]

As seen from the red colored boxes, the intraoperative vascular data registration plays a central role in this system. This nonlinear registration determines the vessel displacements during the brain shift. Therefore, our main objective is to find new methods and techniques to better evaluate these displacements by better imaging, representing the registration data (blood vessels) and removing the outliers present in the registration data. In addition, the full vascular tree classification for Doppler images will be investigated.

Chapter 2 explains the techniques in details.

1.3 GMCAO System and Limitations

1.3.1 Pre-Operative Phase

Before performing a neuro surgery, the patient brain images in the form of MRI are acquired for surgical planning and registration. MRI images are very important in surgical planning as they present detailed information about patient's anatomy. In this system, apart from the traditional MRI images, we will acquire 3D Time-of-Flight Magnetic Resonance Angiography (3DToF MRA) images to acquire brain vascular tree of the patient.

The segmented vascular tree from the patient will be used as the reference for subsequent image registrations with the intraoperative Doppler vascular images acquired during the surgery. This registration is [31-33] very important to measure the tissue displacements during brain shift. Patient specific biomechanical model is built using the MRI data of the patient.

1.3.2 Intra-Operative Phase

In intra-operative phase, surgeon will perform initial registration of the physical patient with the digital patient. In neuro surgery, this is commonly done either using point based registration or surface based registration.

As shown in Figure 1-2, during the surgery, intraoperative Doppler images are acquired using 2D US probe and the sparse vascular data points acquired from Doppler images are nonlinearly registered to the initial MRA vascular tree [31] minimizing the Euclidean distance based energy function proposed in [53]. Remember, the Doppler US only acquire partial vascular data and cannot predict the brain shift accurately in entire brain. The calculated vessel displacements are used as new boundary conditions for the biomechanical model and the model is capable of interpolating smoothly displacements inside the full biomechanical model. Using the deformed biomechanical model, the preoperative images are updated.

1.3.3 Limitations of the System

The initial system developed in [31] has shown the technical feasibility of using a hybrid solution as discussed earlier. However, author [31] claims the registration results that will be the input to the biomechanical model was not accurate enough to realize the brain shift accurately. Therefore, this work will focus on addressing the following limitations of the system.

- No 3D reconstruction of 2D US Doppler images to better represent the imaged vascular region.
- Vascular data are represented by mass centers of the segmented data, which do not guarantee a centeredness representation and do not consider the neighboring data.
- The registration data in both MRA vascular tree and Doppler vascular tree contain outliers and no filtering is performed to remove that.
- The preoperative vascular data and intraoperative vascular data can not be matched being sparse data.

Chapter 2 explains the methods and techniques that will be implemented to provide better registration results.

1.4 State of the Art of Doppler Ultrasound in Brain Shift

Doppler ultrasound imaging for brain shift has been studied in [31-33] successfully and has shown promising results. The work done in [32-33] use intraoperative Doppler vascular data that will be registered to the preoperative MRA data and thereby deform the preoperative data to update the images depicting brain shift. However, the approach of [31] is unique as it uses a hybrid solution where a patient specific biomechanical model is used to update the preoperative MRI data using the displacement field calculated from intraoperative Doppler images. Therefore, it can take into account brain-skull contact boundary conditions, tissue behavior and surgeon interactions.

It is difficult to give a rigorous statement about state of the art of using Doppler ultrasound for brain shift compensation. There are three main validation steps performed in biomedical research.

1. Validate with digital phantom (chapter 7) data,
2. Validate with physical phantom / cadavers data (chapter 2) and
3. Validate with real clinical data. During this study.

The digital phantom results shown in [32-33] will be used as state of the art results to compare the results obtained in this study.

However, it is worth mentioning that the approach we use here is aimed at improving the system proposed in [31]. All the techniques developed in this study will be evaluated and some results will be compared to state of the art where it is possible to generalize a state of the art.

2. Methodology

The particular interest is given to address and improve the techniques and methods used in the red colored boxes in figure 1-2. The following table briefs the methods used in [31] and in the new approach. The main objective of the work is to implement and propose new methods to represent the vascular tree accurately; filtering extraneous data present and evaluate the methods proposed against the state of the art results and the results obtained in [31]. At the end of this work, it will be justified the work carried here can produce very accurate nonlinear registration of preoperative and intraoperative data.

Task	Previous	New
US image acquisition	3D optically localized	3D mechanically tilted – (geometry of acquisition is priorly known)
US image reconstruction	No reconstruction	3D reconstruction of blood vessels
Vessel centerline extraction	-	Propose to extract centerlines
Vessel centerline pruning	-	Pruning of centerline to filter possible outliers before registration
Vascular tree labeling	-	We completely label the vascular tree
Nonlinear registration	Outliers are filtered using a optimization from source image points to destination image points	We include a registration filtering step before registration to remove as much outliers as possible

Table 2-1: Comparing the Proposed Methods

The remaining chapters explain in detail about each of the methods and techniques mentioned above.

3. Doppler Ultrasound Reconstruction

Ultrasound imaging is widely used for medical diagnostic purposes; in monitoring the progress of pregnancy, visualizing tumors, guiding surgical needles in prostate surgeries, etc. Interestingly, with the advancement of the computer vision and image processing techniques, the low-level images such as ultrasound images can be preprocessed efficiently and accurately to give better diagnostic details to surgeons [41-43].

The basic principal of ultrasound imaging is to detect the sound energy reflected by the human tissues. Ultrasound imaging is done in different modes; most used medical modes being B-Mode ultrasound and Doppler ultrasound. The principal of imaging is completely different for those two modes and that inherently decide their medical application. In addition, ultrasound images are available in both 2D and 3D, though full 3D imaging is not widely available. This report will not stress much on the principals of ultrasound imaging, however will detail little about Doppler imaging [44].

Doppler images are increasingly being used as an affordable noninvasive imaging technique for surgical and diagnostic medical applications [45]. Though the early applications were mainly in the domain of vascular disease diagnostic, the recent works suggest larger domain of medical applications; registration, surgical guidance. Doppler methods are unique among ultrasound technologies as it provides both morphological and functional information about an organ. In clinical practice, the interpretation of Doppler signals entails the extraction of information about the blood flow using the confounding factors of conventional Doppler theory.

3.1 3D Ultrasound reconstruction

Though there are complete 2D array of transducers to acquire 3D ultrasound images, the cost of such systems are high and not available in most clinical facilities. The conventional 2D ultrasound imaging systems are widely available and it is a basic component in any clinical facility. For applications where 3D images of organs can provide better details, stack of 2D US images can be used to reconstruct the 3D features of the acquired region [47-48].

3.1.1 Methods of 3D ultrasound imaging

There are different ways to acquire a stack of 2D images for 3D ultrasound reconstruction that are being widely used.

1. Two-dimensional array of transducers
2. Mechanical devices
3. Sensor based free hand 3D imaging

Since, surgeons have shown concerns about offering line of sight to the optical trackers and the time consumed, this report is focused mechanical trackers though a full mechanical tracking system is not yet available at TIMC-IMAG. However, the available ultrasonix mechanically tilted

probe (Fig 3.1 b) can be used to mimic the same acquisition functionality of a mechanical tracking system. However, spatial tacking is not offered, which means the images are acquired corresponding to the ultrasound image coordinate system of the probe.

A series of 2D ultrasound images are acquired by moving the probe mechanically over the anatomy using a motor. The movement is either a rotation about a fixed axis or a translation in some direction. Since the scanning protocol is predefined, the geometric orientation of each acquired image is precisely known in space. Different types of scanning are given in the Figure 3.1.

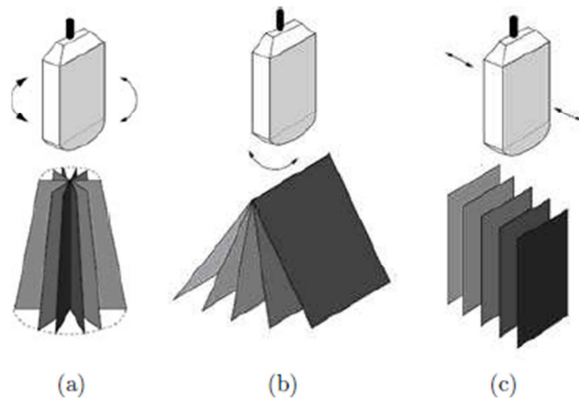


Figure 3-1: Different geometries that can be acquired from mechanically moving the probe. a) rotational b) tilted c) translational, Source [69]

3.2 Power Doppler Acquisition

The Power Doppler images are acquired from a mechanically tilted ultrasound probe (Figure 3.1 (b)) using the ultrasonix system available. The ultrasonix system allows to acquire a set of images by tilting the transducers by known angles, thereby allows to acquire a known Field of View (FOV). Since, the geometry of the acquisition and the position of each image are known, these images can be used to reconstruct the actual 3D volume in a voxel space.

3.2.1 US image geometry

The ultrasonix imaging interface Propello allows the communication with ultrasound probe and set the imaging parameters of the acquisition. The images can be acquired in manual or automatic mode; either individual or stack of images can be saved. The saved image set complies with a simple protocol that can be used to read the image file; a header with geometric parameters of acquisition, binary stream containing image data.

The following figure shows the fan like image data set's geometry that can be acquired using the ultrasonic mechanical probe.

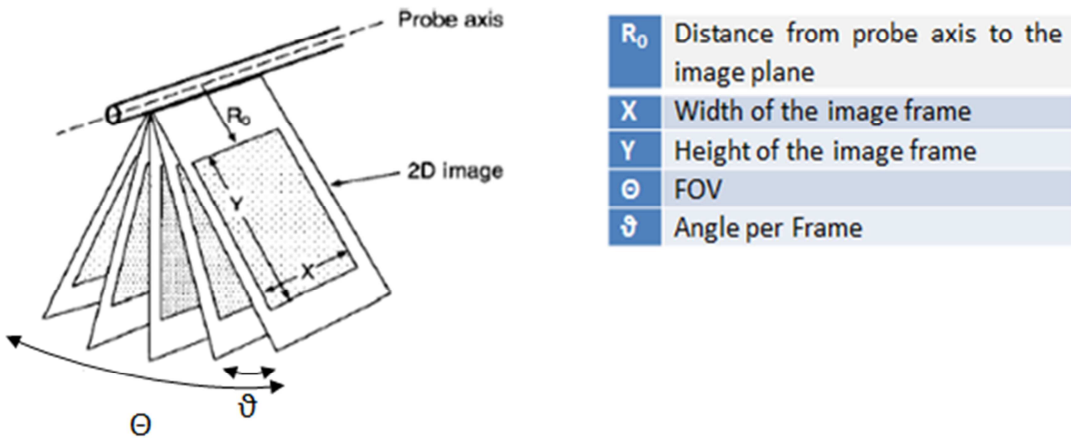


Figure 3-2: US Image Geometry

The image parameters used were $X=484$ px, $Y=364$ px, $\theta=0.73^\circ$ and $\Theta=84.68^\circ$.

3.2.2. Individual US image preprocessing

Individual Doppler images consists both Doppler data and B mode data where B mode data are gray scaled ($R=G=B$) and Doppler data are colored. Simple filter was applied to separate the color pixels from the gray scale pixels. This filter first converts the Red-Green-Blue (RGB) pixels to Hue-Saturation-Value (HSV) pixels and then set the pixels with saturation equal to zero to zero. Following this segmentation, the color pixels were converted to gray scale pixels to convert color Doppler images to gray scale images. The converted image set was used for the 3D reconstruction of the Doppler vascular tree. In addition, it is worth noting that there was no threshold done after converting Doppler color images to the gray scale images since it can lead to remove inner pixels of the vessels and this can eventually lead to holes inside vascular branch.

3.3 3D Reconstruction of Doppler Vascular Tree

Cartesian 3D reconstruction of the Doppler volume acquired from the propello® raises two concerns; one is correct coordinate transform from Cylindrical to Cartesian coordinate system and correct interpolation to recover the lost image data during acquisition [49-51].

3.3.1 Image Data and Coordinate Systems

The individual Doppler images are 484×364 pixels with a physical spacing of 0.144mm. The image stack acquired will be in a cylindrical coordinate system centered at US transducer. The reconstruction should get this stack of images to a 3D voxel space to represent it in a 3D image. The image coordinates are in Cartesian space and these Cartesian coordinates should be transformed to the cylindrical coordinates and vice versa. Figure 3-3 shows the corresponding image coordinate systems.

The physical imaging origin is chosen as O_0 , which serves as the reference coordinate system for transforming 3D image voxels to corresponding physical points and thereby to the corresponding US image pixels.

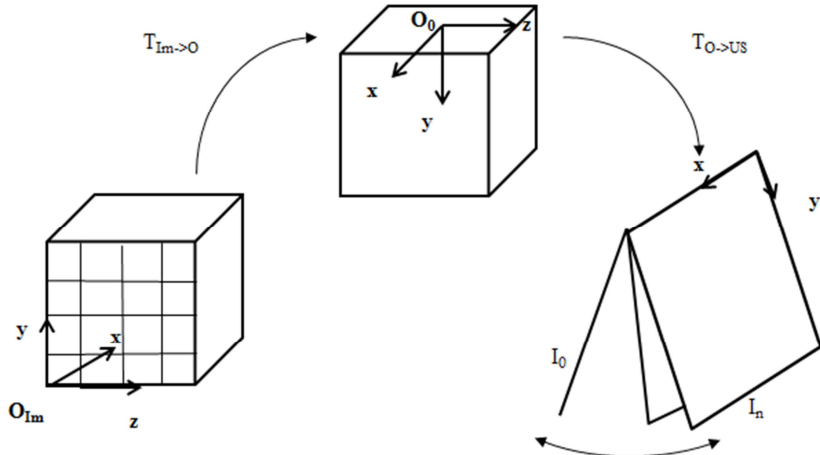


Figure 3-3: Image Coordinates and Transformations

Given a 3D voxel (i,j,k) , the corresponding physical coordinate (x,y,z) (in the reference frame) can be found by simple image transformations. The transformation of homogeneous image point to reference frame, $T_{Im \rightarrow O}$,

$$T_{Im \rightarrow O} = \begin{bmatrix} -S_x & 0 & 0 & W/2 \\ 0 & -S_y & 0 & 1 \\ 0 & 0 & S_z & -L/2 \\ 0 & 0 & 0 & 1 \end{bmatrix}$$

Here, W - 3D image x -extent, L – 3D image y -extent, S_x , S_y , S_z are corresponding image spacing which are set to 0.144 mm (spacing of the US images) for reconstruction.

3.4.2 Mapping Physical Point to US Image Data

The US image data serves as the source image set for the 3D reconstruction, where the 3D Cartesian image is the target image. Since, the underlining geometry of the source and target images are different, voxel-to-pixel mapping (backward mapping) or pixel-to-voxel mapping (forward mapping) should be carried out. The backward mapping is selected for couple of reasons;

- Pixel-to-Voxel mapping will introduce fair amount of multi mappings (which will depend heavily on the spacing selected) due to the cone like image data representation of the actual US data.
- Inefficiency occurs due to multi mapping and related interpolation in target domain after mapping. (The figures below will show the requirement for expensive interpolation kernels.)
- Possibility of setting Region of Interests (ROIs) in 3D image to be reconstructed from the image stack.

The US image set can be physically represented as a set of 2D planes centered at origin O_0 to represent the actual physical planes imaged by the US transducer. A given voxel can be either fall onto a plane, in between two planes or to none of the planes. This helps to reduce the number of mapping and coordinate transforms that has to be calculated. In that, only first two coordinates of the cylindrical coordinates (r, θ) , which correspond to a point (x, y, z) is necessary to determine whether the voxel in consideration being imaged by tilted US probe or not. Please notice the actual 3D image contains the tilted US image set and US image set occupies only a partial area.

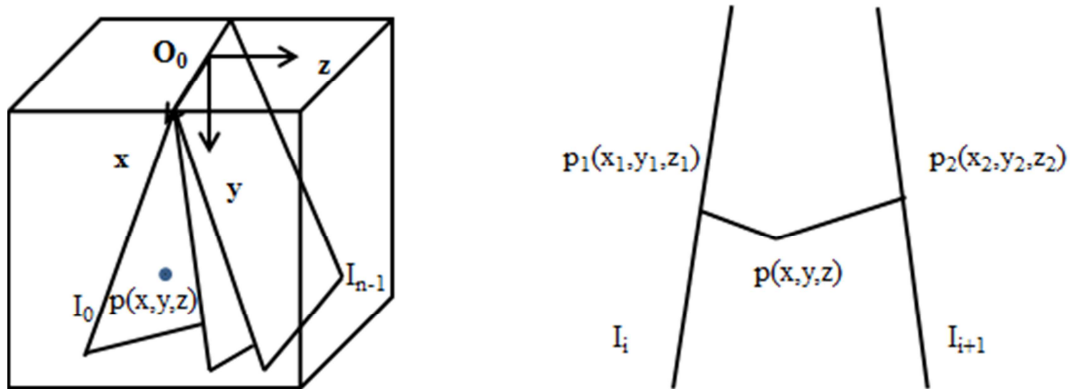


Figure 3-4: Embedding US image planes inside 3D volume (point is between two planes)

Given a point (x, y, z) , the first two coordinates of the cylindrical coordinates (r, θ) can be easily calculated using the formula;

$$r = \sqrt{(y^2 + z^2)}$$

$$\theta = \tan^{-1}(z/y)$$

The radius r along the virtual plane containing the point (x, y, z) will decide if the voxel is out of imaging radius R_0 of the US imaging. In this way, considerable number of voxels is avoided before the interpolation is carried out.

The incline θ will decide whether a voxel is; on an image plane, out of FOV or between two image planes. The planes corresponding to actual images are stored with their corresponding incline angle. This map can be used to retrieve the corresponding image plane/planes for point (x,y,z) (Figure 3-4).

If the point (x,y,z) is in between two planes (I_i and I_{i+1}), the point will be projected to the two image planes and there by the corresponding closest plane points will be retrieved (p_1, p_2).

Given a projected point $p_1(x_1, y_1, z_1)$, the corresponding image point $(x_{us,1}, y_{us,1})$ in the 2D US image can be found;

$$x_{us,1} = x_1 + W/2$$

$$y_{us,1} = \sqrt{y_1^2 + z_1^2}$$

$$I_{us,1} = I_i$$

Same true for $(x_{us,2}, y_{us,2})$ and will be used to find the corresponding image points for the point p (x, y, z) . Remember a point p can fall exactly onto an sparse image plane, in which there will only be $p_{us,1}$. Above relationship allows mapping a given voxel (i, j, k) in the 3D image to the corresponding US image plane points.

3.3.3 Interpolating image data

When correct geometric mapping of a 3D image voxel to the US image pixels is known, it is important to use a good interpolation technique to approximate the intensity of the voxel from the sparse data. In this, the interpolation use is a combination of bilinear interpolation and distant weighted interpolation.

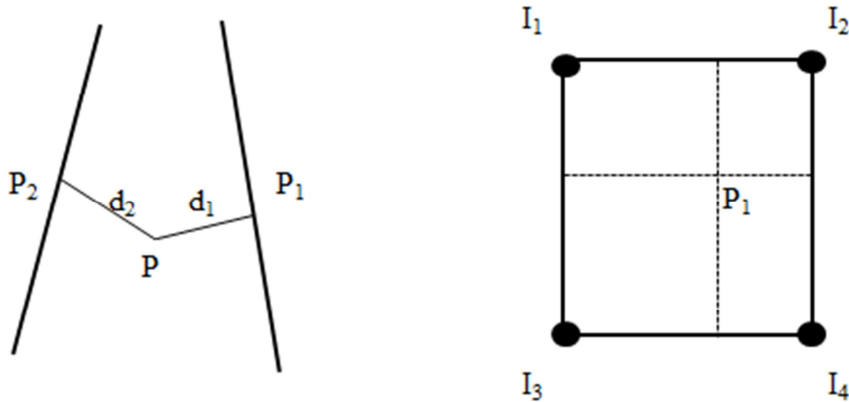


Figure 3-5: Distance weighted and bilinear interpolation

Figure 3-5 shows a situation where the voxel P is projected to points P_1 and P_2 on the two corresponding US image planes. The intensity of P_1 and P_2 is calculated using a bilinear

interpolation (typical equation in a 2D image). The actual voxel intensity, I can then be calculated using a distance weighted interpolation using I_1 and I_2 calculated at point P_1 and P_2 respectively.

$$I = \frac{I_1 * d_2 + I_2 * d_1}{d_1 + d_2}$$

The 3D image can be reconstructed computing each voxel value as discussed above. Though, there is also a possibility of using higher order interpolation techniques like splines, our results show this reconstruction technique is fast and robust. The results are shown to prove that the reconstruction was very accurate and the subsequent processing made the results much better removing reconstruction artifacts.

3.4 Reconstruction of Synthetic Data

To understand the reconstruction algorithm performance, the first step performed was to use synthetic data in the same geometry without noise added. This allows evaluating the reconstruction performance with known conditions.

3.4.1 Synthetic US Generation

To get the synthetic images in the same geometry as the actual Ultrasonix ultrasound probe, a virtual US acquirer was developed in Matlab. This completely allows the mechanically tilted image acquisition of known geometric objects or 3D images (ex. Angiography taken from MRI). The only drawback is mimicking the noise accurately.

Importantly, the objects or images can be placed in different known depths and can be used to study the different aspects of 3D reconstruction. As the first step, the virtual acquirer was used to acquire images of known geometric objects like spheres, tubes and boxes, which has sharp and smooth edges. The results below show the results of the reconstruction and the results are very good. Also, the error of reconstruction was measured manually for the parameters like sphere, tube radius and bow width and height. The error is negligible and this proves the reconstruction accuracy in a perfect acquisition conditions without actual US effects.

3.4.2. Interpolation artifacts in Synthetic Data

It is very important to understand the interpolation artifacts that will lead to overestimate or underestimate the reconstruction of the blood vessels. The estimations in any interpolation will cause artifacts depending on the structures being reconstructed. However, knowing the structures being reconstructed can be used as a way to study the estimation error and thereby to understand the ways to correct that.

The parameters of the image acquisition which are typically of the numbers given in Figure. 3-2, it can be easily seen the maximum separation of the data points are of $364 * 9 = 4.63$ pixels. This shows the image data are relatively dense. However, the interpolation can overestimate the

vessels and also can lead to merge close vessels depending on how close they are. These situations are carefully studied using virtual spheres and further image processing is applied to avoid the artifacts. Because, the imaging is done in a cylindrical coordinates where the individual image plane has a 2D regular grid, the spacing along the radius is given by $r^* \theta$, which depends with how far the points are from imaging origin. This implies the distance-weighted interpolation will vary along the radius. The overestimation of the spheres is quite symmetric and will not need any processing. However, as depicted in Figure 3-6 there can be situations where, the two tubes can be connected which, will lead to problematic centerline representation of the tubes. This, situation is avoided selecting a distance based erosion. These values were set depending on the practical results.

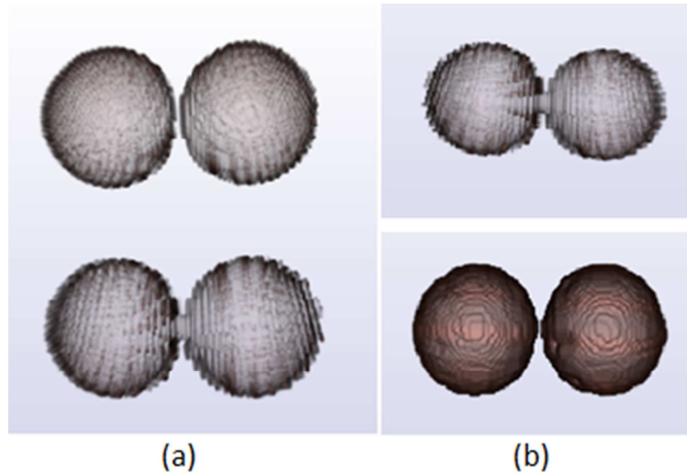


Figure 3-6: (a) Reconstructed spheres 2pixel apart and along the y-axis (b) removing the connected sphere using radial erosion

The figure above shows along the y-axis, spheres that are 2 pixels apart, are connected for the higher y coordinates. This is apparent since the DW interpolation overestimate more along the y-axis. To overcome this, a radial based erosion was applied and the size of structuring element was selected to be 1 for 0-100 range, 2 for 100-200 range and so. This also allows removing the connected vessels that can be arisen for actually touching vessels.

The Figure; 3-6 (b) shows the clear reconstruction of the connected two spheres after radial erosion is applied and respective dilation to recover the actual data and threshold to get the binary image.

3.6 3D reconstruction of phantom data

3.6.1 Building the Phantom

It is important to evaluate the algorithms and techniques developed on phantom data before applying them on the clinical scenario. Doppler phantoms are used to evaluate the Doppler US imaging techniques developed. As a preliminary phantom, the following requirements were identified;

1. Simulate the blood flow
2. Allow blood flow medium to be shifted

In [52], a comprehensive illustration is given to build a phantom that can simulate brain shift. Here, the phantom developed is technically very similar to the one in [52]. However, this phantom will only be used to evaluate the 3D reconstruction accuracy and thinning algorithm.

Roughly, the phantom consists with following materials and features;

- Deformable phantom with Agar.
- Saline tubes as Blood vessels (3.2 mm).
- A catheter bag to understand the brain shift.
- A harvard pulsating pump was used to pump the water (blood simulant) in to the saline tubes (blood flow medium)

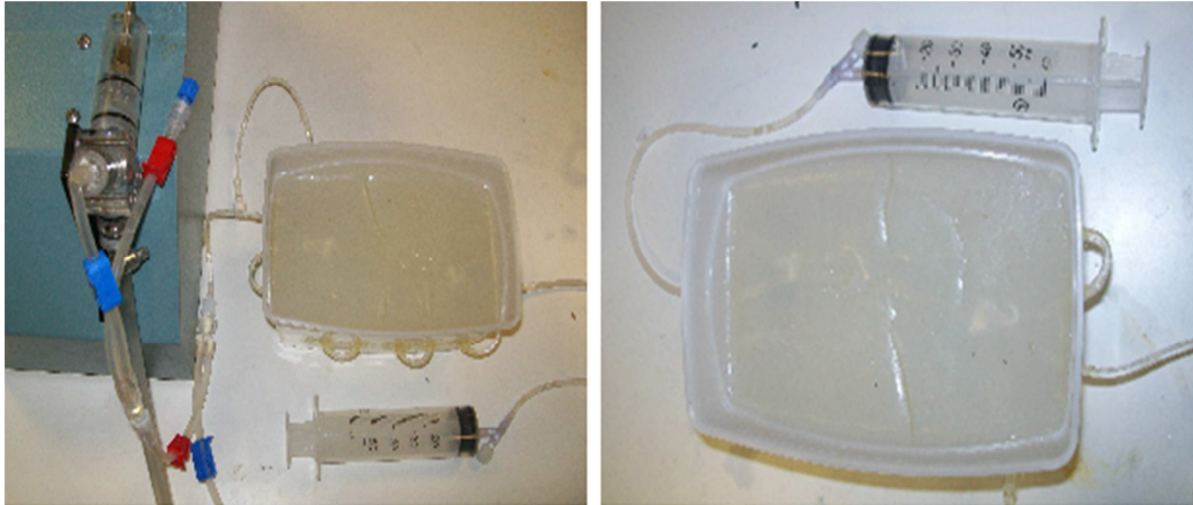


Figure 3-7: Physical Phantom

3.6.2. Reconstruction results and evaluation

The tubes used to simulate the blood flow were of the size 3mm. The images were acquired and reconstructed as explained in the previous chapters. The reconstructed phantom blood vessel

diameter was manually measured to evaluate the mean and standard deviation of the reconstruction.

These results show the effect of deformation, occlusion and reconstruction of US imaging and reconstruction. The 100% deformation cause one vessel to be completely out of the US acquisition region in this situation.

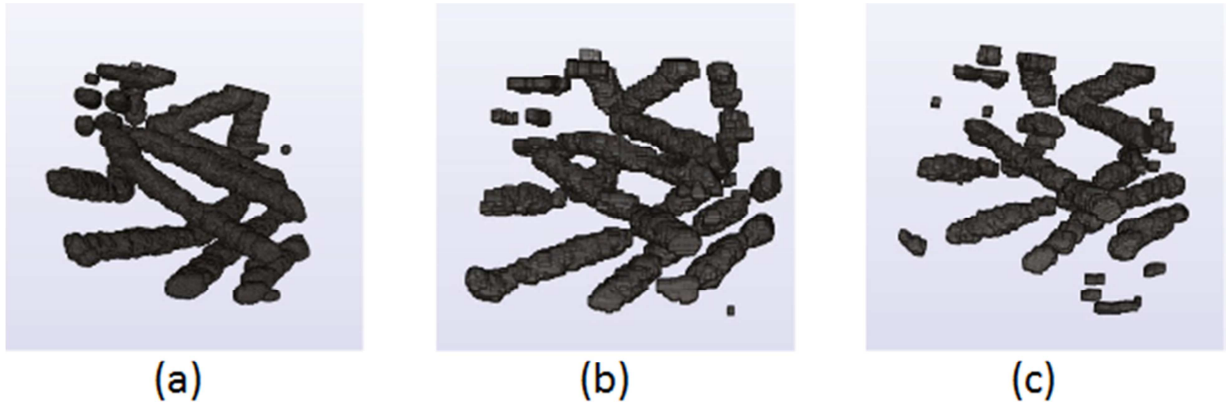


Figure 3-8: (a) reconstructed tubes (b) reconstructed tubes after 50% liquid applying catheter balloon (c) deformed after 100%

The diameter of the vessels were measured manually and it was found the mean diameter is about 3.43 mm after dilating and smoothing while it is 3.39 mm before dilating and smoothing. Standard deviation of the diameter after dilating and smoothing the volume was 0.49 mm while the standard deviation before dilating and smoothing was around 1.2 mm. It is apparent from the above non-smooth results the deviation in the diameter is quite big as smoothing even out the tubular structure.

Note the error will also depend on the flow produced by the Havard pump, which in our practical experience was not functioning accurately. The oscillation frequency of the pump was very different from the one that was indicated on the pump display. However, this will not be a concern for other work that has been done during this thesis.

4. Vessel Topological Skeleton Extraction

As discussed in Chapter 2, the cerebral vasculature [31-33] has shown promising results as an intraoperative registration structure for brain shift compensation. The cerebral vasculature is distributed all over the brain cortex and inside the brain. During brain shift the vessels are found to be deforming much in the same way as local tissues. Therefore, vasculature can be used as a good candidate to capture the brain shift [31-33]. Chapter 3 discussed a method, which completely reconstruct 3D vascular tree of a ROI using Doppler ultrasound and the results were interestingly accurate. The brain shift can be evaluated by non-linearly registering the preoperative (MRI Angiography) and intraoperative (Doppler Angiography) vascular image data. There are different techniques for nonlinear image registration. However, we are interested to evaluate and improve the registration method proposed in [53] by adopting a better representation of vascular data for registering and filtering the extraneous vascular data.

To extract the source and destination image points for the registration, we can extract the curve skeleton (cf. 4.1) of the 3D vessels, which will describe the topology and geometry of the vessels. Though there are claims that it would be better to use complete 3D vessel-to-vessel registration [33], the test carried out in [31] shows it is not. Our main motivations to use the medial axis of the vessels are,

- They topologically describe the 3D shapes
- Further processing is possible to improve the registration accuracy
- This compact representation allows faster registration and better results.

4.1 Topological Skeleton of Geometric Shapes

The topological skeleton [54-55], sometimes used interchangeably with the notion of medial axis (App. A.1) [67], is the thin version of the geometric shape that is equidistance to its boundaries. Skeleton emphasizes the geometric and topological properties of the shape under consideration. Shape representation using the topological skeleton have shown applications in many areas of Computer Vision, Computer Aided Design, Biomedical Engineering and etc. [55] In discrete shape representations of 2D and 3D objects, the shape is represented by a finite set of simple elements, such as points, line segments, and/or planar faces.

Skeletonization:

Conceptually, Skeletonization is seen as a function $S^{n,m}$ that assigns a m-dimensional components that are in R^n space to an n-dimensional shape embedded in an R^n space. In this work, we are considering the 3D space where n=3 and the Skeletonization assigns a m=1 components to describe the shape, which is commonly known as curve skeleton.

Curve skeleton:

The curve skeleton (C), is a one-dimensional skeleton $S^{3,1}$ of a 3D shape. The curve skeleton represents the 3D shape as a thinned and centered set of connected curves. Figure 4.1 represents a curve skeleton of a 3D vessel.

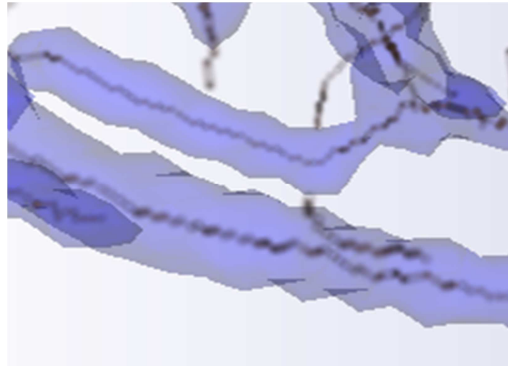


Figure 4-1: Curve Skeleton of the Vascular Tree

4.1.1 Skeletonization by Thinning

There are different approaches studied by different authors [55] for extracting the skeleton of shapes; Thinning, Voronoi Diagrams, Distance Field and Hybrid Approaches. In this work we use the thinning method proposed in [56] to skeleton extraction which allows to extract the skeleton, preserving topological and geometrical properties. The work in [58] has shown robustness of this algorithm for medical data.

Thinning also referred to as erosion and binary peeling is an iterative process, which aims to erode the object surface until the skeleton remains. Thinning methods exist for both curve and surface skeletons. The basic idea is to classify the object points and remove the simple points, which does not change the topology of the shape [56-57]. The method is iterative, where removal of simple points introduces new simple points until the method converges to the skeleton. Some thinning methods do not necessarily preserve the geometric properties of the shape while others maintain both topological and geometrical properties of the shape by maintaining endpoints that are on the tips of the significant skeleton parts.

There are two major approaches to image thinning: a) kernel-based filters and b) decision trees. Kernel based approaches filter the image based on structuring elements, which classifies the points and can be extended to higher dimension. On the other hand, decision trees are only limited to 2D and 3D image thinning but offer fast thinning algorithms.

Every thinning method relies on voxel classification for removing the simple points. The method in [56] consider all possible combination of 26-neighbourhood, that is 67,108,864 using the decision tree. However, the final curve skeleton is not guaranteed to be one voxel thick for each curve points and depends on the object being skeletonized. So, further processing needs to be carried out to make the curve skeleton one voxel thick and to remove the skeletal noise.

4.1.2 ITK implementation of the Thinning algorithm

Insight Segmentation and Registration Toolkit (ITK) possesses a complete algorithm implemented strictly as discussed in [56]. ITKs developed algorithm [58] was used for image thinning and the algorithm was tested to see the centeredness of the skeleton curve to justify the choice of this algorithm to represent the 3D vessels. However, the method will not be evaluated against other algorithms.

4.2 Results of the Image Thinning

First, the MRA cerebral vasculature that will be used throughout this work was skeletonized. Here it should be mentioned that Dr. Luca Antiga freely provided a complete vascular tree of MRA data from his PhD work.

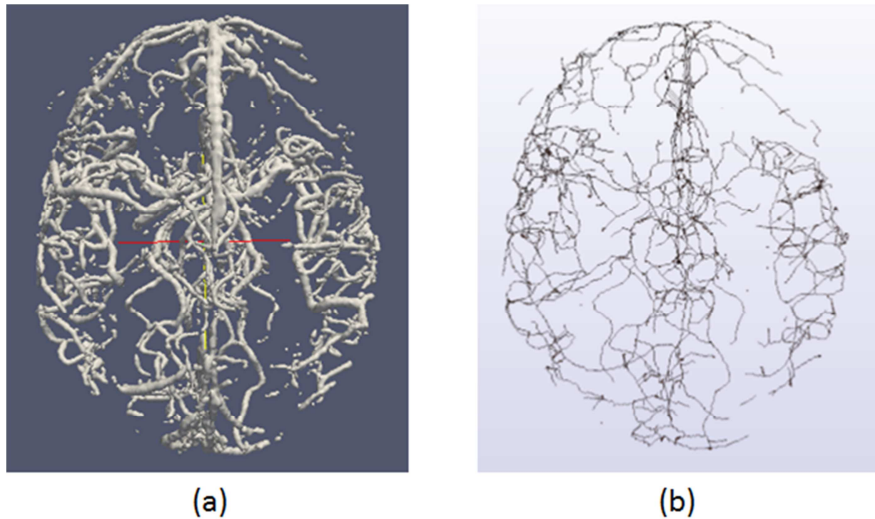


Figure 4-2: (a) MRA segmented cerebral vasculature (courtesy of Antiga) (b) Skeletonized cerebral vasculature

Figure 4.2 shows the output of the `itkImageThinnning` filter which is a 3D binary image. The skeleton contains considerable amount of spurs (noise). In addition, there are very short vessels, which will have to be removed before using MRA vascular tree as the reference registration data.

Figure 4.3 shows thinning of 3D reconstructed vessels from the phantom. The amount of noise is almost close to 5% of the actual centerline data. There are considerable amount of spurs, isolated small branches and undesirable connections that represent the noisy data. This can be as much as 5%-10% of the desired data in some cases where the reconstruction will not be accurate due to noise and occlusion occurring in Doppler acquisition.

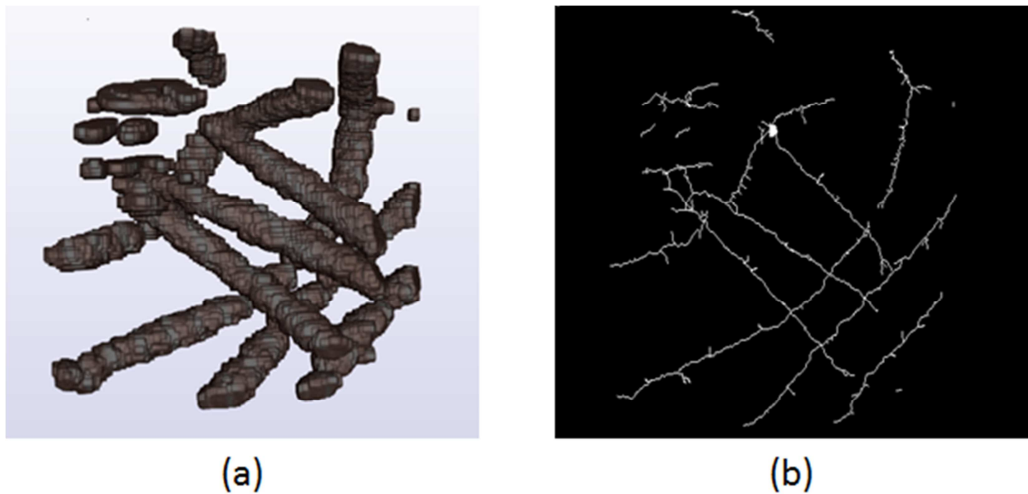


Figure 4-3: (a) Doppler Ultrasound reconstructed phantom vessels (b) Skeletonized phantom vessels

It is very important to remove the outliers present in registration data to get a better registration result that will accurately measure the deformation of vessels during surgery. Removing such outliers is known as “Pruning” [63].

5. Elastic/Nonlinear Image Registration

Image registration is a fundamental area of research in computer vision and image processing, which is widely used in many image-based applications [59-60]. In simple terms, registration can be seen as spatially aligning two images of a scene. This allows investigating the subtle changes in different images or image data under consideration. The complexity of finding an accurate and robust registration function depends on its application. Image registration has long been studied and adopted in medical imaging to understand and evaluate different clinical aspects using different imaging modalities ranging from MRI, CT, US, X-ray etc.

5.1 Registration Workflow

Typical image registration involves the steps shown in Figure. 5.1. Following figure describes the different steps and how they are treated in this work.

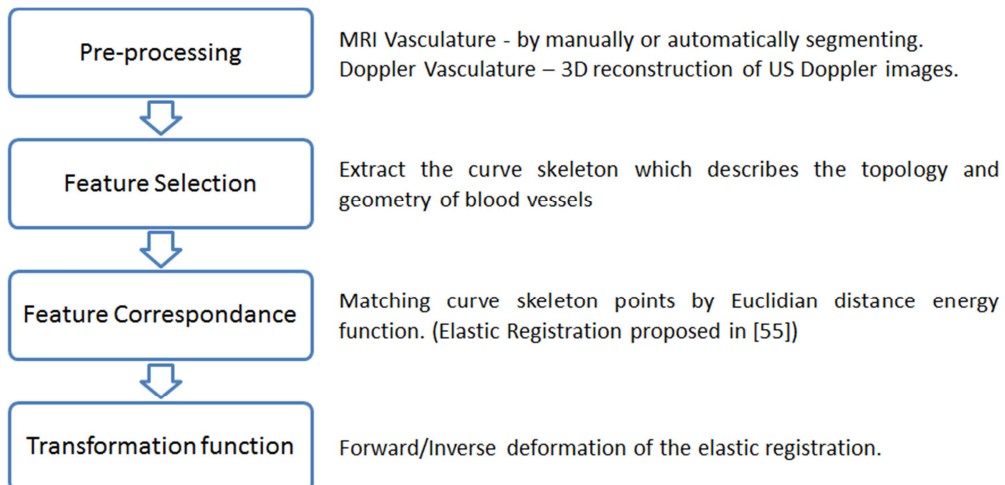


Figure 5-1: Registration Workflow

5.2 Elastic Registration

Elastic registration algorithm should establish a correspondence between the sparse, incomplete, redundant and noisy intraoperative configuration (source) of the vascular tree and the clean, complete pre-operative (destination) representation of the same structure.

5.2.1 Registration Overview

The Elastic Registration function is a mapping R that register source data set and destination data set. Here the data sets considered can be seen as a point cloud of the curve skeleton. The registration tries to minimize Euclidean distance between the S (source) and D (destination) data points by iteratively minimizing the energy function defined on a regular elastic grid.

Consider the point cloud is embedded in a 3D grid and the grid is deformable. The deformation R is formed by successive elementary grid deformations r . The regular grid can be deformed in order to minimize the registration error (minimize the Euclidean distance between two point sets).

The optimal registration is achieved by progressively refining the grid points. Corresponding registration function after j steps,

$$R = \underbrace{r_J^{N_j} * \dots * r_J^1}_{G_J} * \dots * \underbrace{r_1^{N_1} * \dots * r_1^1}_{G_1}$$

Here G_j , $j=1,\dots,j$ are the successive grid refinement and r_i^i , $i=1,\dots,N_j$ are the elementary deformations performed at each level. Remind that the number of elementary deformations in different levels have no correspondence.

R can be expressed in compact form as;

$$R = r_N * \dots * r_1$$

$$\text{where, } N = \sum_{j=1}^J N_j$$

Using this formulation the registration error can be minimized using elementary deformations applied to grid nodes at successive steps. The subdivision of the regular grid is performed when no registration minimization is possible in the given configuration.

With the above definitions, the registration energy E that should be minimized to find the similarity between source and destination point clouds can be formally expressed. The energy is defined as the sum of Euclidean distances between source and destination data points in order to sought the geometrical similarities.

At step n the energy is defined as;

$$E(r^n * R_{n-1}) = \sum_{s \in S} d(r^n(R_{n-1}(s)), D)$$

Here,

R_{n-1}	Registration function assembled at n-1
$d(\dots)$	Distance function, in this case point-to-point distance

From a computational time point of view, a distance map can be generated to accelerate the algorithm using the destination point set D similar to the work proposed in [61].

5.2.2 Energy Minimization

The idea of elastic registration is to find the best registration to map the source data set S to the destination data set D. The energy is defined in terms of Euclidean distances.

The iterative evaluation starts with embedding destination point set in a regular elastic grid. Energy is successively minimized by subdividing the elastic grid to regular hexahedrons. The basic idea is to consider the grid nodes separately and apply the deformation to reduce the energy until there is no energy minimization possible at the current grid subdivision.

Take S_0 initial source points set, and S_i the source points set at iteration step i . The node, which leads to the maximum energy minimization of all the nodes, is displaced while all other nodes remain fixed. The displacement is smoothly propagated through the neighboring grid cells (Ex. 4 neighboring cells in 2D) to collect the new source points set S_{i+1} .

After each deformation step, the elastic grid is returned to its original regular position and the new points set S_{i+1} is embedded in the original grid again. This allows fast computations and easy interpolations.

The iterative energy minimization procedure is terminated when no significant energy minimization can be achieved by any of the nodal displacements. In [53] the stopping criterion T_E is set to 1% reduction of the energy, $(E_i - E_{i+1})/E_i > T_E$.

5.2.3 Grid Subdivision

The energy minimization can be localized iteratively by iteratively subdividing the grid. The section 5.2.2 discussed how the energy minimization can be achieved in a given grid refinement level.

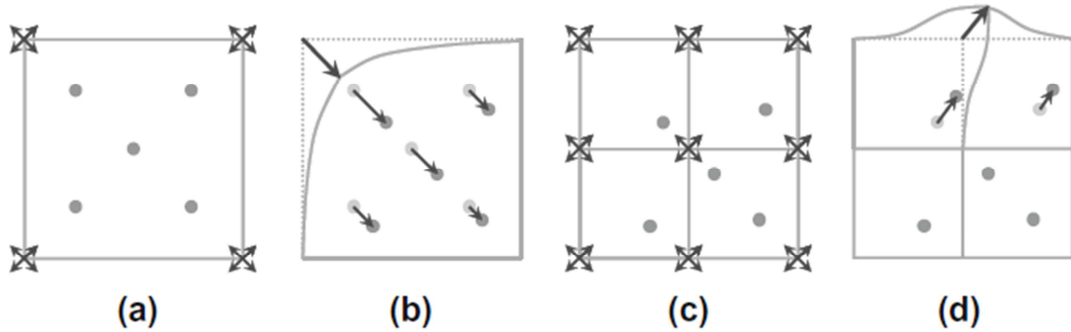


Figure 5-2: Elastic Registration (a) S_0 at refinement level 1 (b) S_1 after deformation at level 1 (c) S_1 at refinement level 2. (d) S_2 after deformation at level 2, Source [53]

The iteratively assembly of source points set S is illustrated in Figure 5.2. In this figure, only the source points are shown for clarity reasons. In (a) the initial source points set is embedded in the initial elastic grid without subdivisions. The global energy function is calculated for Euclidean distance and the energy gradients are calculated at the four nodes of the square. The optimal node displacement is applied in (b) and the source points are displaced to create the current configuration S_1 . If no further energy minimization can be achieved at level 1, the gird is refined.

The source points S_1 in (c) is embedded in the new grid refinement level 2. Here the energy gradients at nine nodes are calculated. The best nodal displacement minimizing the energy is applied in (d) generating new source points set S_2 .

The full algorithm and optimization strategies used are thoroughly explained with examples in [53].

The algorithm relies on a forward-backward filtering technique to filter the outliers of the source points set where the miss matches are removed by cross checking of source and destination data.

5.3 Qualitative Analysis of the Algorithm

The algorithm explained above for elastic registration was applied to the phantom data set acquired by mimicking the brain shift. The results are shown in Figure. 5.3.

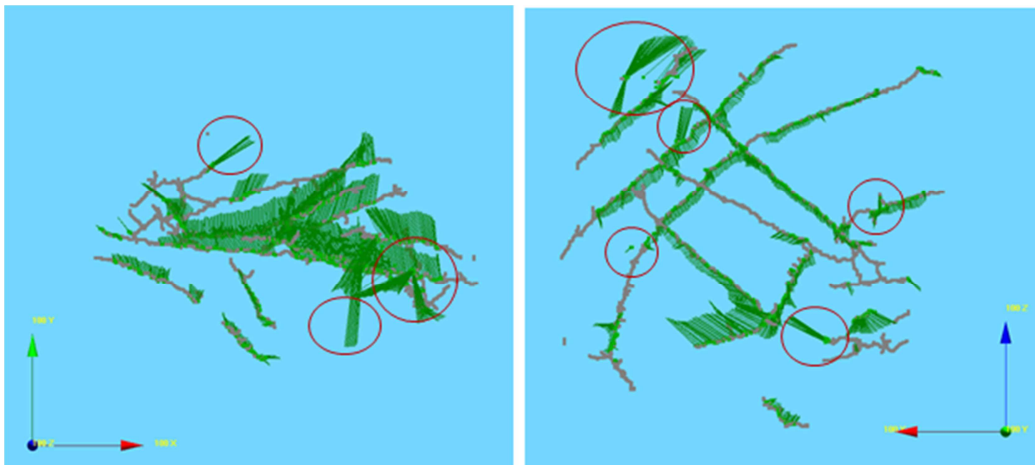


Figure 5-3: Registered results the green lines show the displacement vectors of individual source points on to the destination points. The red circles show possible miss registrations due to noise data.

Remarks:

Bear in mind the deformation caused in phantom is a physical deformation which is nonlinear yet smooth;

- The displacement vectors circled in the figures does not comply with the neighboring displacement vectors.
- In addition, there are some small vessels causing uneven deformations.
- Most of all, the destination data contains noise and very small vessels after thinning algorithm.

Therefore, it is necessary to apply a filtering step before the registration is performed for both destination and source curve skeletons.

6. Registration Filtering and Enhancement

As seen from the previous chapter extraneous data present in both destination and source curve skeletons can largely contribute to unwanted point displacements, which will lead to non-smooth and excessive deformations. To avoid this situation it is necessary to apply a filtering step for the reference MRA curve skeleton as well as the intraoperative curve skeleton of Doppler images. The main filtering step is to apply a pruning and short vessel deletion step to remove the noise present in curve skeleton.

6.1 Curve Skeleton Pruning

As discussed in chapter 4 there is no thinning algorithm available in the literature, which can produce curve skeleton free of noise. Therefore, pruning [62] is often necessary to remove the noise present in the curve skeleton. It is very important to make sure pruning only removes unnecessary branches present in the curve skeleton. Most common way of pruning the skeleton that is being used in available toolkits is to simply apply a threshold and remove that amount of voxels or pixels from the branch ends. This leads to unnecessary shortening of the significant branches and does not consider branched noise curve skeletons (this situation will be discussed later). Therefore, it is necessary to develop new techniques to prune the curve skeleton.

Though there has been considerable work done on 2D skeleton pruning [63], in 3D only a few methods are proposed and some are only applicable to special scenarios and others are brute force algorithms [64]. In this chapter a new voxel classification based pruning algorithm is introduced which works in noisy curve skeleton pruning.

Importantly the algorithm is developed for nearly thinned curve skeleton containing surface skeleton parts. All the thinning algorithms are not guaranteed to provide a one-voxel thick curve skeleton and will provide curve skeletons with two voxel width parts. This is particularly case for the distance map based thinning algorithms. In addition, during this work it was found that there could be surface skeletal parts present in the curve skeleton due to the noise in the actual image volume in the form of holes. For noisy images like Doppler reconstructed volume images studied in this work, there have been situations where the curve skeleton contains surface skeleton parts.

However, the algorithm removes surface skeletons if they are bigger than actual vessel size. This never occurred during the work and is not likely to happen. In the section 6.1.5.3, this is explained in detail and a possible solution is given.

6.1.1 Digital Topology

The geometry of a 3-D digital image (2D case is similar) \mathbf{I} is a subset of \mathbf{Z}^3 . Object of interest in a digital image are represented by a non-empty subset \mathbf{S} that consist of all the voxels with value 1. Given a voxel point $p = (i,j,k)$, following neighborhoods are defined.

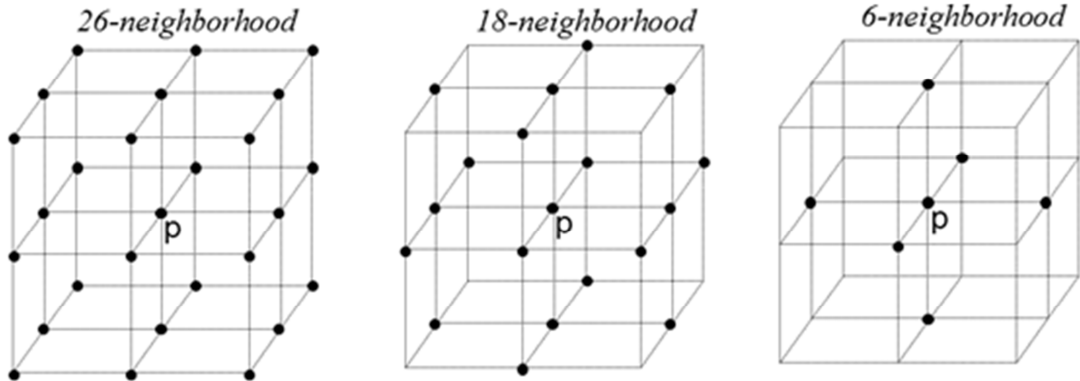


Figure 6-1: Three types of neighborhood in a 3D image

6-connected-neighbors: if two points share a face

18-connected-neighbors: if two points share a face or vertex

26-connected-neighbors: if two points share either a face, or a vertex, or a corner

The connectivity analysis is very important in pruning and vascular tree labeling. As there are three types of possible connected neighborhoods, three types of connectivity can be defined as n-connectivity. The connectivity determines whether a set S is connected or not. If the considered connectivity is 6-connectivity, for a set S to be considered connected, there should be a path between any two voxels, which can be reached using 6-connectivity.

If the object is, a curve as is the case for curve skeletons there can only be three types of voxels present. Object is represented by 26-connectivity.

End Point – Only one neighbor

Path Point – Only two neighbors

Joint Point – More than two neighbors

Therefore, a vascular branch is a 26-connected point set starting from a junction point and traverse until an end point. Vascular labeling tries to label all the branches present in the vascular tree with or without their corresponding lengths.

6.1.2 Pruning Workflow

As seen by the flow chart below, the pruning algorithm accepts a 2D or 3D curve skeleton as its input. The first step is to analyze the skeleton voxels in their most basic connectivity representation in a graph data structure. Then, the curve skeleton will be classified to junction points, path points and end points. The noise is removed using the algorithms and classification explained below and the new vascular skeleton is represented with the connectivity information.

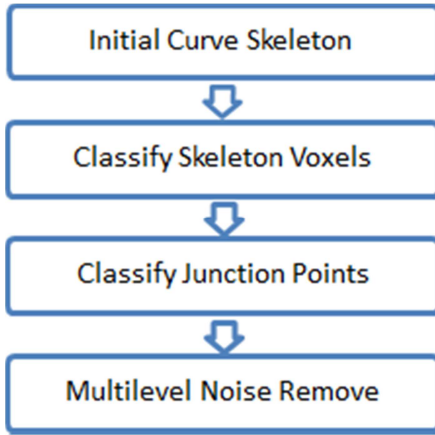


Figure 6-2: Pruning Flow Chart

6.1.3 First Level Curve Skeleton Classification

It is important to classify the connectivity of all the curve skeleton voxels in a given 3D image as the first classification step. This classification as discussed in 6.1.1 only considers the number of 26-neighbors connected to a given voxel. After this classification step, all the object voxels are classified either end points, or path points, or joint points. The classified points are stored together with their connected points in a graph. In addition, branch points and end points are stored in a different list for fast access for traversing and classifying. Since these data structures only contain the pointers to the actual skeleton data, new changes can be made immediately.

Why first level curve skeleton classification is not sufficient:

The junction shown in Figure 6.3 (a) is a simple (perfect) junction point where a voxel emanating three branches where those path points are not 26-connected. However, skeletonization algorithms cannot guarantee the curve skeleton only contains simple junction points. This happens due to the junction point will not shrink to a one voxel. Figures (b) to (e) contain junction clusters.

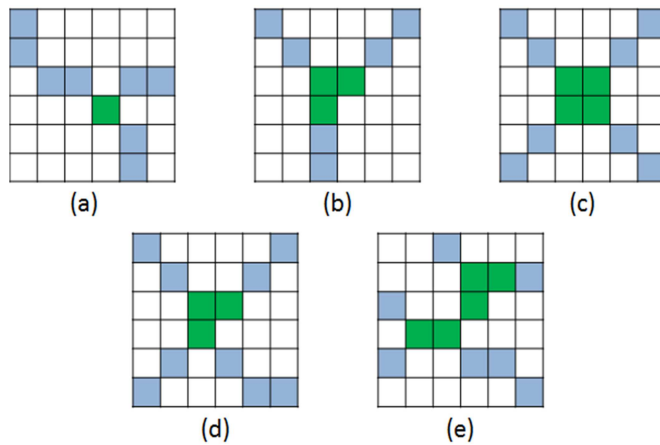


Figure 6-3: Branches emanating from junction points (green), blue represents path points

There are some approaches proposed in [63-64] to mark actual junction voxel from a junction cluster but they will fail at situations like (d) and (e). In addition, the algorithms do not guarantee the most natural junction voxel.

In this work, we try to find the most natural junction point from a junction cluster focusing on 3x3 clusters for 2D and 3x3x3 cluster for 3D. The junction clusters extending beyond this value cannot be generalized very easily to a geometric solution. For, those situations the algorithm will divide the junction cluster to sections and will find junction points. However, this is very unlikely in lot of situations. Through this work, no such situation was encountered.

However, before classifying the junction clusters, the algorithm removes noisy branches present in the vascular tree. This allows removing or changing the junction points, which emanate noisy branches and thereby give better classification possibility as the junction clusters will likely be changed to much simpler clusters.

6.1.4 Noise Removal/Pruning

After the step of classifying junction, the classified endpoints and path points can be used to traverse through the curve skeleton. This allows simple traversal along the vascular tree data structure to analyze the vascular tree.

Noisy (insignificant) branches and short redundant paths are removed by traversing through the graph created in the above steps. The threshold length of the noisy branches and redundant branches are set to the diameter of the vessels.

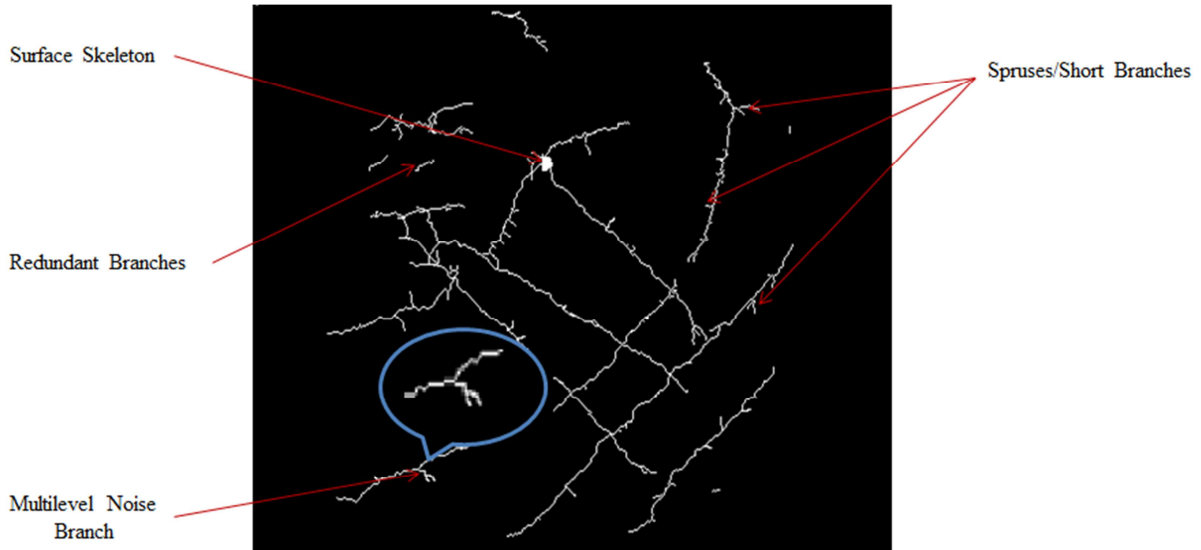


Figure 6-4: Skeleton Noise Described and Surface Skeleton Shown, blue circle is a zoomed multilevel noise branch

The multilevel noise branches are not addressed or indicated in the literature [62-64]. The term multilevel noise is introduced here for the branches that will be emanated from significant

skeleton curve and then will be branched again in a junction to make more branches, however the effective length of the particular segment is less than the noise threshold (zoomed in Figure 6.4).

The noise removal is carried out through the graph data structure created and updated until this step. There are two choices for traversing to check whether the branch is a noisy spruce or not. One is to start traversing from junction points and the other is to start traversing from endpoints. The option of traversing from endpoints was selected since it will allow removing spruce branches and redundant branches in one pass. If junction points were selected for noise removal the noise in the form of endpoint-to-endpoint should be removed again traversing starting from endpoints.

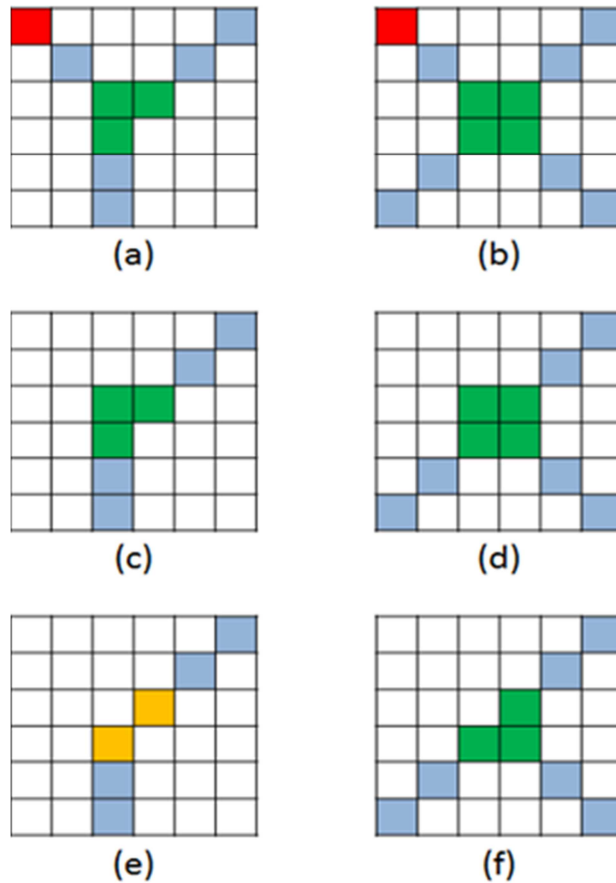


Figure 6-5: (a-b) Junctions before noise removal; (c-d) Junction after noise removal; (e-f) Junction points are removed if it does not affect the topology. (Red points are end points)

Figure 6-5 (a) (b) shows a situation where the junction cluster contains small noisy branches (red are end points). Figure 6-5 (c) (d) shows the noise removed skeletons. Note that after removing the noisy branch, skeleton still contains junction clusters, which can be further skeletonized (thinned), that is, removing them does not disconnect the curve skeleton. To remove these junction points at each noise removal path when the path encounters a junction point, the junction point is checked. The junction point is removed if the removal does not disconnect the curve skeleton. This is shown in Figure 6.5 (e) (f) where two junction points are removed from Figure

6-3 (c) (d). Also, note if the junction point is converted to an end point after this step, a noise check starting from that end point is performed. This allows multiple noise branch removal in the presence of junction cluster in the noise branch.

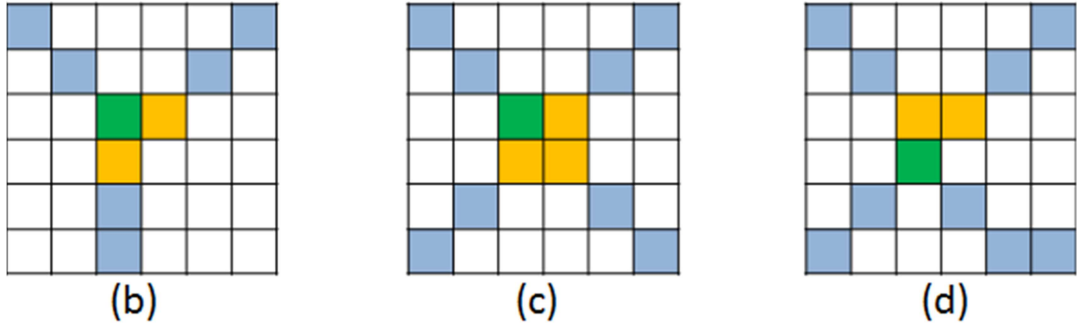


Figure 6-6: Classified Junction Clusters, (b) (c) (d) are letters of the initial branch clusters from Figure 6.3

6.1.5. Classify Junction Clusters Completely

Contrary to most approaches proposed [62-64], here the importance is given to classify the junction clusters fully to identify a junction with a single junction point.

6.1.5.1 Classify 3x3x3 Junction Clusters to a Simple Junction

This section explains how a junction cluster of 3x3x3 is converted to a simple junction. The classification works as explained below. The branches connected to the (path points) junction cluster are recorded. Then from each junction point the accumulative distance to each path point is calculated in 26-connectivity. The junction point with the minimum accumulative distance to path points is selected as the junction point and remaining junction points are converted to path points and marked as converted junction points (yellow) for traversing purpose. If there are more than one junction points with the minimum accumulative distance, as the junction point a random point is selected among those. (Figure 6-6 (c) and (d)).

6.1.5.2 Classify Larger than 3x3x3 Junction Clusters to a Simple Junction

If the junction cluster formed looks like the one in Figure 6.3 (e), the situation is handled by first dividing the bounding box containing junction cluster into two. Accumulative distance calculation is changed as follows. Important thing to notice is now there can be junction points outside the bounding box. The distance from a junction point to a junction if the traversal is through a junction point as seen in Figure 6-7 (a) is set to infinity (red line).

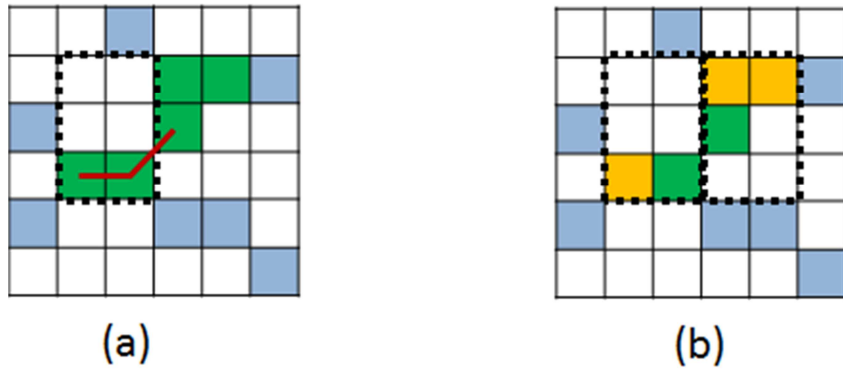


Figure 6-7: Multiple Bounding Box Approach

6.1.5.3 Converting Skeleton Surface to Junction and Path Point

Because the Doppler images reconstructed can contain noise, there can be holes present in the volume. Thinning will produce surface skeleton for this particular situations. It is necessary to convert these surface skeletons to curve skeletons. The technique used is explained below.

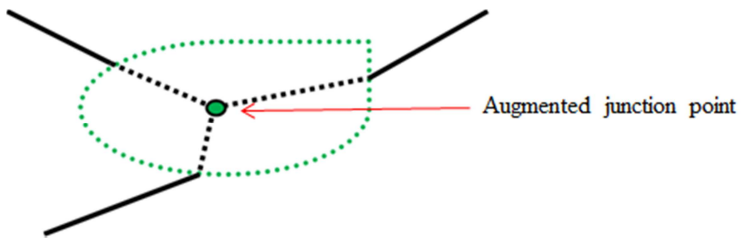


Figure 6-8: Augmenting Junction Point at Surface Skeletons

The Center of Gravity (CoG) of the surface skeleton is calculated and the junction point is augmented at CoG as in Figure 6-8. The path branches connected to surface skeleton is connected to the augmented point using the shortest path calculation in the digital image.

However, if the surface skeleton was bigger than some threshold (vessel diameter) this method would generate line like skeleton, which are not natural. To this end, it will be possible to implement a better junction point algorithm taking care of the curvature of the branches emanating from the surface skeleton and finding their best intersecting point. This is not implemented here and luckily, there were no surface skeletons bigger than the vessel diameter size.

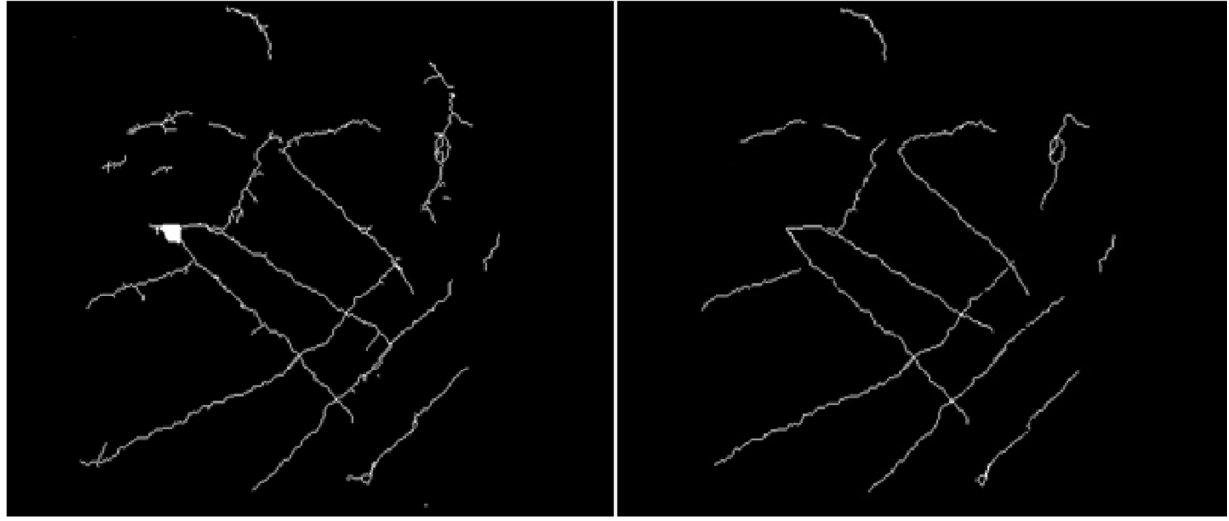


Figure 6-9: Phantom Vessels (a) Unpruned (b) Pruned

6.1.6 Vascular Tree Labeling

The steps described above builds a curve skeleton free of noise and junction clusters, which can be used to classify the vascular tree fully. Vascular tree classification has been studied in different studies [65-66]. However, it is important to create a noiseless curve skeleton to better label the vascular tree. The chapters explained above creates a nice noiseless vascular tree that can be used to label the branches of the vascular tree (Figure 6-10). In a vascular tree, this work anticipates three following types of vessels.

- Vessels from junction point-to-junction point (Full Vessels)
- Vessels from junction point-to-end point (Half Vessels)
- Vessels from end point-to-end point (Disjoint Vessels)

To classify the vascular tree it is necessary to iterate through the vascular tree starting from junction points. The junction points used here are updated junction points from the previous steps. The implementation is not detailed due to space requirements of the report. However, the idea is to iterate from each branch point to label the Full Vessels and Half Vessels according to their start and end point types. The vessel lengths and vessel labels emanating from each branch are recorded and stored. The junction points finally contain the branch labels and their lengths emanating from them. In addition, when branch is labeled the corresponding end points are recorded.

To label the disjoint vessels, the important information is the endpoints recorded in the previous step since those end points are not contained in a disjoint vessel. Next, the algorithm traverses thorough remaining end points which are guaranteed to be in a disjoint vessel. All disjoint vessels are recorded and stored this way.

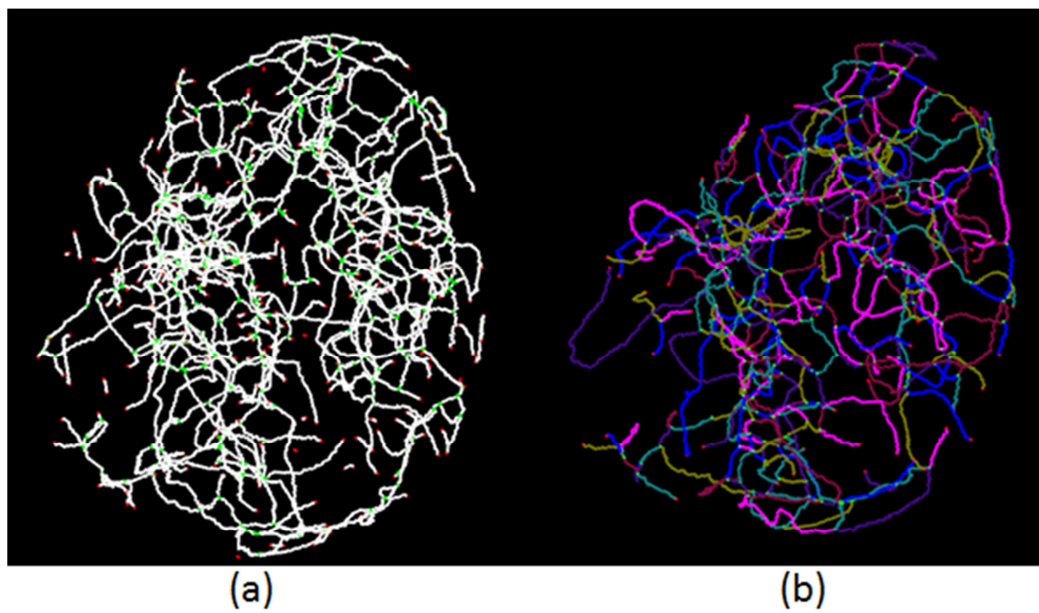


Figure 6-10: MRA Vascular Tree Prunned and Labeled

Figure 6-10 (a) shows the initial MRA vascular tree with noise present. Figure 6-10 (b) shows fully labeled vascular tree. Each branch is represented by a different color.

6.1.7 Centeredness of Thinning Algorithm

The centeredness of the thinning algorithm was evaluated after the curve skeleton was pruned (App. A.2). This allows better evaluating the centeredness as no noisy data will contribute to the centeredness. The evaluation was carried out for the reconstructed phantom data. The maximal ball that can be embedded to the reconstructed 3D image at curve skeleton path points were calculated and their average and standard deviation saw very good results. The diameter of the reconstructed phantom tubes were 3.43mm.

The diameter of the tubes measured at curve skeleton path points averaged to 3.36mm with a standard deviation of 0.69mm which prove the centeredness of the results are very close to the actual values.

7. Synthetic Data Generation and Synthetic Brain Shift

As the first step to validate and evaluate the proposed algorithms, this section introduces a digital phantom representing the Doppler US vasculature and to simulate a vasculature deformation (computed with a known analytical deformation). The process tries to synthesize the Doppler US from the available MRA data and tries to get a close representation to that of the actual Doppler US.

7.1 Qualitative properties of actual Doppler US

It is important to understand the qualitative properties of actual Doppler US images to synthesize them using the MRA data already available. By carefully observing the Doppler and MRA images of blood vessels, the following qualitative properties were found to be interesting while developing synthetic Doppler US.

1. **Thick:** It is seen the Doppler US vessels are thicker than the MRA ones. One possible explanation is that the signal gain is increased while acquiring the Doppler images in order to allow smaller and distant vessels to be imaged.
2. **Noise and Artifacts:** Random scattering and reflection of the US signals produces artifacts.
3. **Uneven:** The US vessels are found to be uneven and the reason for this is probably the distance from the probe.
4. **Occlusion:** Some vessels are not seen entirely because of occlusion by other vessels on their imaging path.

7.2 Digital Phantom

The digital phantom simulates the appearance of Doppler vasculature by taking MRA vasculature as the input image. Figure 7-1 describes the steps involved in the synthetic data generation process.

It is important to note that contrary to the synthetic data generated for brain shift simulation in [33] (where the data is generated by purely adding noise to MRA volume), in this work the virtual US probe is used to acquire and to reconstruct US volume with the virtually acquired US image set from the MRA volume.

The vessels acquired from the process shown above can mimic the Doppler vessels and their properties. An analytical deformation can be easily added to the deformed vessels to simulate the brain shift. In addition, it is possible to apply the simulated brain shift to the original MRA volume and then to acquire an US image set using the virtual probe of the new MRA data. Therefore, the process and tools developed are very flexible and can be used to totally simulate the actual scenario in a surgical room.

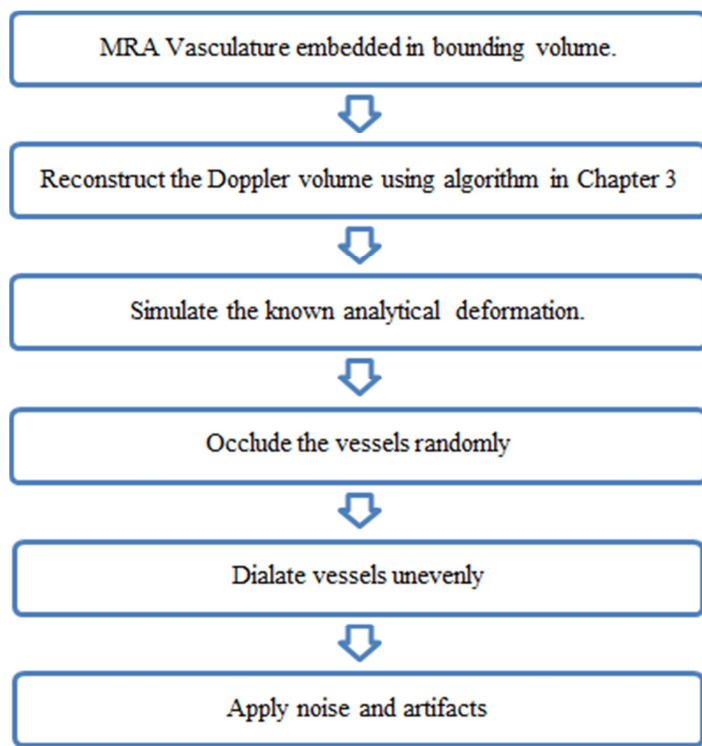


Figure 7-1: Simulate Data Generation

8. Evaluation and Discussion

In previous chapters, the results of the algorithms were mentioned with evaluations. In this chapter, the algorithms and methods developed will be evaluated in the same way they will be used in the GMCAO system. The methods that discussed so far mainly aimed at developing new techniques for improving the intraoperative and preoperative image registration during the surgery. The evaluations given in this chapter is performed on digital phantom data that was discussed in Chapter 7.

8.1 Evaluation Platform

The Figure 8-1 and 8-2 shows how the evaluation data was generated and the TRE (Target Registration Error) of the registration was measured. Here, the following intraoperative (simulated) data was generated simulating the brain shift by deforming the vascular data. Therefore, the initial point locations ($P_{initial}$) are known before registration.

1. 2D US vascular data without 3D reconstruction
2. 2D US vascular data with 3D reconstruction and without noise removal
3. 2D US vascular data with 3D reconstruction and noise removal
4. Actual MRI data

As seen in Figure 8-1 destination registration data is the initial MRA vascular tree's centerlines after noise is removed.

The source registration data will be synthesized in order to evaluate the above-mentioned 4 criterions. As ground truth, the brain shift will be simulated on the MRA vessels itself, so this will only be a nonlinear deformation done on MRA data. These data are without any noise, occlusion and reconstruction artifacts and serve as the best candidate for ground truth.

The deformed vascular data of above four types will be registered to the initial MRA vascular tree and the registered point locations ($P_{registered}$) are recorded using the registration software.

The TRE is easily calculated as $P_{initial} - P_{registered}$.

All together 15 tests were performed with different amplitude of deformations ranging from 5mm to 40mm. This counts for around 3000 data points per test. Therefore, all together 45000 data points with different deformations were extensively tested to understand the statistical distribution of TRE error. The TRE was calculated by applying the deformation field computed in registration to get the initial positions of the vessels (Figure 8-2) before deformation.

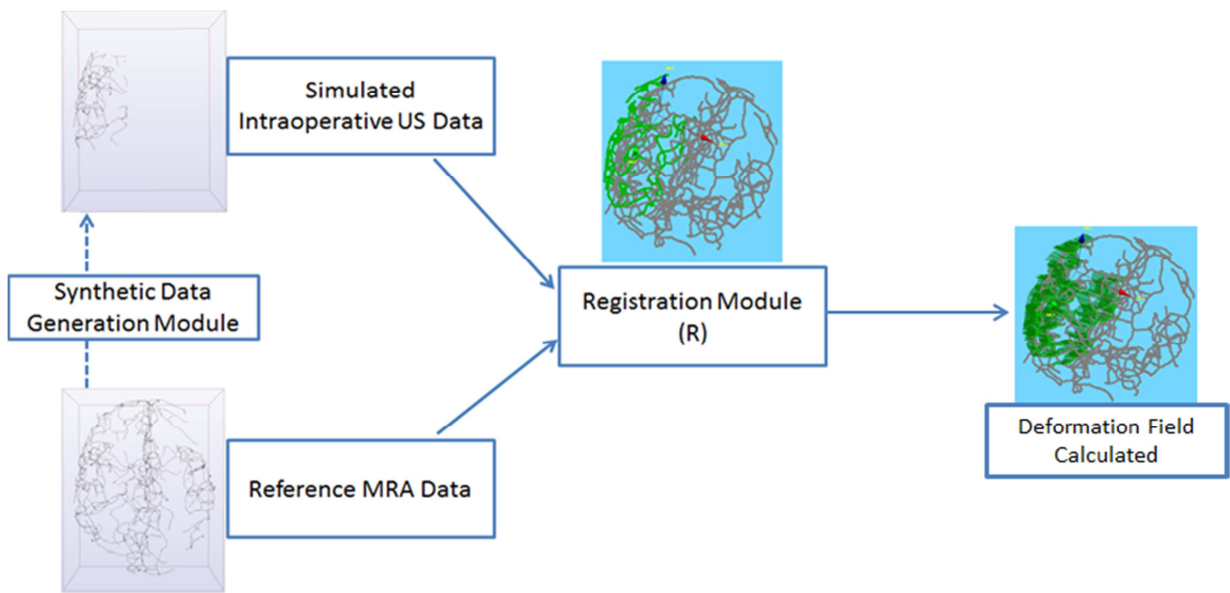


Figure 8-1: Registration Workflow

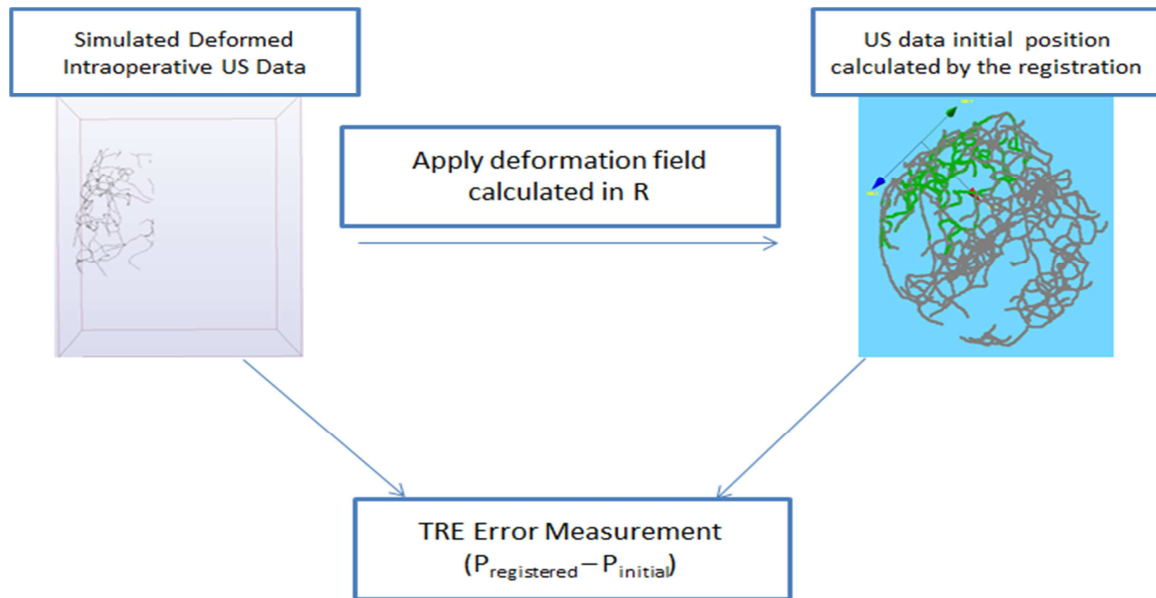


Figure 8-2: TRE Measure Calculation

8.2 Results

The successful registrations were considered as the registrations with TRE less than 1.5mm that is a very accurate result. The graph below shows the percentage of successful registrations for different data generated.

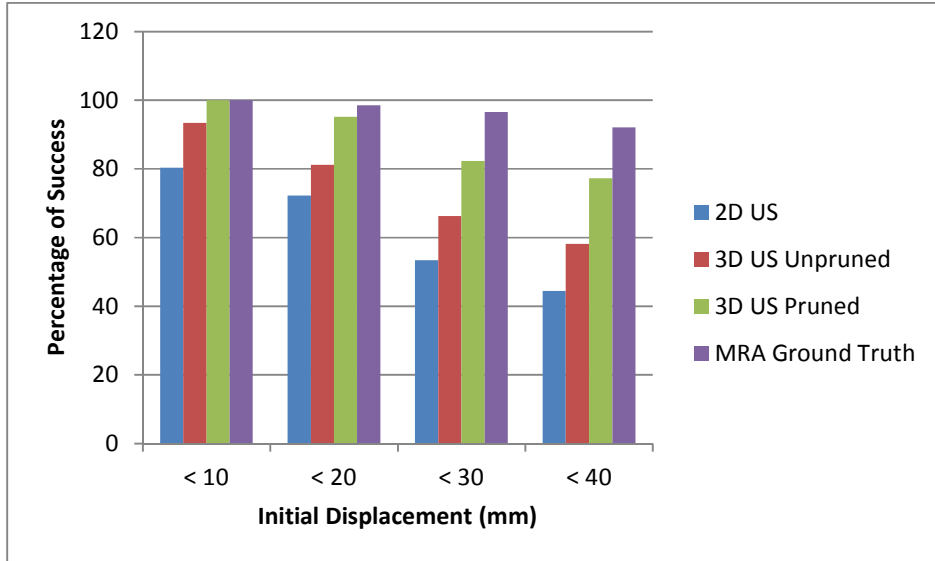


Figure 8-3: Digital Phantom Registration Success for different misalignments

The graph clearly shows the improvement of using 3D US contrary to 2D US. 2D US successful percentage drops to 50% if the misalignment is in the range of 40mm. The reason is as the data points are sparse and no correspondence is present the nonlinear registration algorithm miss register data as the primary criteria is the Euclidean Distance energy whereas for 3D data the dense points will be aligned accordingly at the subdivision levels of the registration algorithm.

The pruned (Green) version of the 3D US data shows very good successful registration percentage as the local registration points are not affected by the extraneous data present in unpruned data (Red).

The registration filtering is very successful as the results obtained here shows considerable improvement in the success ration compared to the results shown by [33] for their digital phantom which is 70% for misalignments of less than 35mm whereas the results here were 75.3.

In addition, it is worth mentioning the registration algorithm developed in [53] performs accurately. This can be seen as the MRI ground truth data has a registration success percentage of 92% even after 40mm misalignments.

The next test that was carried out was using the labeling of vascular tree to check if that can increase the success registration. As initial work, the interest is given to see if there is an increase in the registration accuracy of using only the full vessels (Junction Points-to- Junction Points) only for the registration contrary to vascular tree containing half vessels (Junction Points -to-End

Points). Figure 8-4 shows a simulated vascular tree where half branches is shown in white. The results were tested on the pruned centerline data.

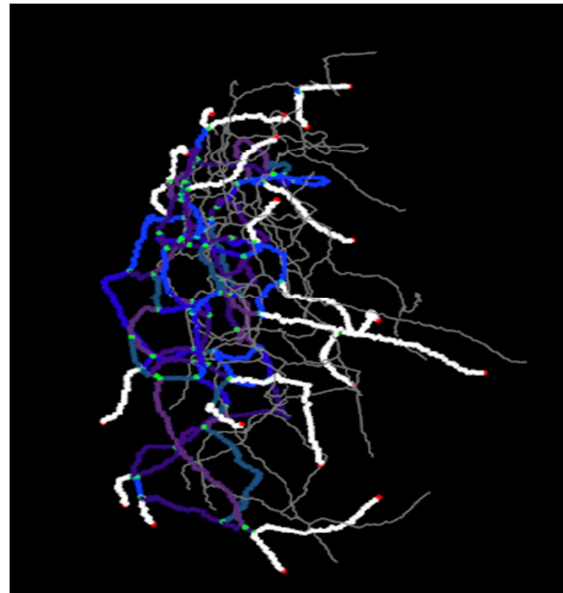


Figure 8-4: Full and Half Vessels (Half Vessels are white), the deformed vascular tree is shown in gray

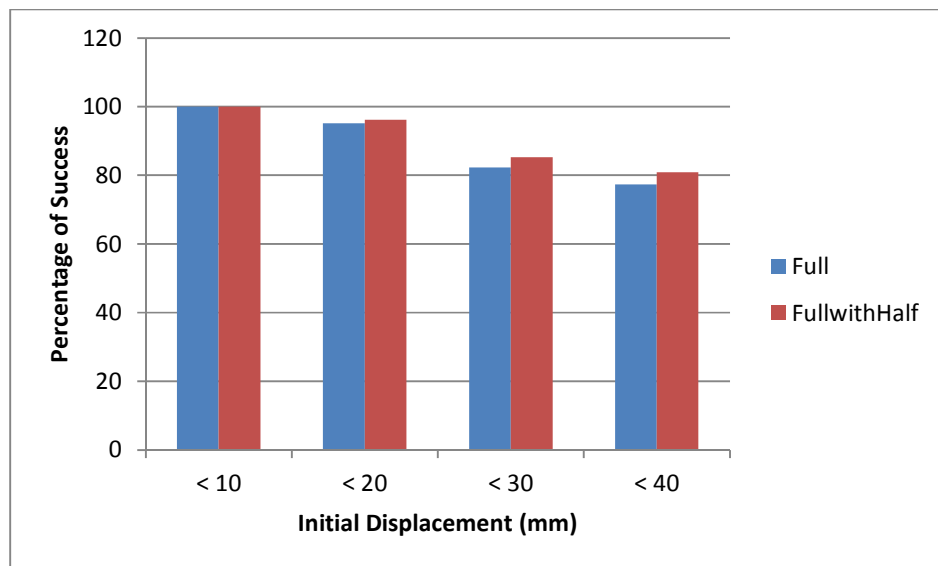


Figure 8-5: Registration Successful Percentage on Full vs. FullwithHalf Vessles

The results above shows a slight improvement of using only full vessels and it is about 4% and does not change a significant difference with the amount of misalignment.

8.3 Discussion

The results obtained in this work clearly shows the significant improvements of nonlinear registration by better representing Doppler US vascular tree (by 3D reconstructing) and removing outliers of the centerlines of the US vascular tree and reference MRA vascular tree. In addition, the digital phantom results are 5% better than the claimed results of [33].

Interestingly, the results of using only the Full vessels of the pruned vascular tree centerlines show considerable improvement in the registration success percentage. This encourages further matching of vascular data before registration is performed to see how the registration improves with the matching of destination and source vascular data. The classification algorithms are already developed in this work to fully label the vascular tree with their corresponding lengths.

The digital phantom data is a good initial evaluation step to ensure the techniques developed actually improve the registration accuracy. However, phantom and clinical data should be extensively used to further evaluate the algorithms and understand the possible improvements that can be made.

9. Conclusion

This work mainly focused on improving the intraoperative registration accuracy of the brain-shift-compensation using Doppler US images, which will be integrated to the system proposed at GMCAO, TIMC-IMAG in [31].

The intraoperative Doppler data was reconstructed accurately and was evaluated with phantom developed to simulate blood flow. It can be advised here to use mechanically tracked probes for Doppler acquisition during the surgery as the results obtained with mechanically tilted probe showed very good results. Interestingly the reconstruction could be further improved by mosaicking [68] volumes reconstructed at spatially different locations since the correspondence is simple between two images as the each image stack acquired contains in a fixed cylindrical coordinate system. In addition, using multiple volumes acquired at different spatial locations will compensate for the occlusions and blood flow changes during acquisition.

The centerlines of the 3D vascular data were used as a candidate for representing the actual 3D vessels, which allows reducing registration data dramatically. In addition, the post processing of centerlines can reduce the extraneous data present in the registration data and can classify the vascular data fully. The algorithms were tested on both phantom and simulated data extensively to check the robustness. However, it is worth mentioning some improvements can be done mainly when there are surface skeletons present in the curve skeleton. The pruning algorithm developed does not depend on the skeletonization algorithm used and this allows easily integrate new skeletonization algorithms or to test other skeletonization algorithms on vascular data. It should be advised that other skeletonization algorithms should also be tested in future to use the better algorithm.

The digital phantom developed allowed simulating the brain shift and 3D reconstruction of intraoperative Doppler ultrasound. The registration results obtained with digital phantom showed clear improvements compared to other digital phantom tests done in the literature. With these results, it can be advised to reconstruct the 3D vascular data from intraoperative Doppler images using the implemented algorithms. In addition, centerlines extraction from 3D vascular data, noise removal of centerlines and labeling of vascular tree improved the registration accuracy considerably.

The full labeling of vascular tree was developed for both MRA data and simulated US data. In future vascular matching algorithms should be developed to match the intraoperative vascular data [66] with the preoperative vascular data. This will further improve the registration accuracy as the exact matching data can be fed to the registration module and thereby miss registration can be avoided while point to point matching. In addition, research should be carried out to investigate if the junctions of the vascular tree are more rigid during the brain shift. This will

show directions to investigate if the junction points can be used as control points during the registration.

It should be mentioned that the algorithms developed above should be tested on different vascular structures. During this work, it was not possible to manage time to gather clinical data other than the MRA full vasculature provided by Dr. Luca Antiga. On the other hand, though the tests performed showed fast computation times, the algorithms should be reviewed to see the possible improvement that can be done software wise.

The next step of this work should be extended to develop a better physical phantom [52] (extending the capabilities of the phantom developed in this work) that can mimic possible surgical scenarios, for example, brain shift, tissue resection. This will allow using the biomechanical model proposed in GMCAO system to evaluate the physical brain shift using the registration results provided by the algorithms developed during this work. Importantly, this will allow mechanical properties especially of tissue resection to be integrated to the biomechanical model for brain shift compensation.

To conclude, the results shown in this work further proved that intraoperative Doppler ultrasound imaging could be used as a strong intraoperative imaging candidate for brain shift compensation. Doppler ultrasound imaging present more advantages compared to its major disadvantages, low quality data and small field of view. The further developments of the technologies investigated during this study aims to bring GMCAO system feasible to use in clinical environment.

References:

1. Kelly, P. J., "Computer-assisted stereotaxis: new approaches for the management of intracranial intra-axial tumors," *Neurology*, 36, pp. 535-541, Apr.1986.
2. Morita, A. and Kelly, P. J., "Resection of intraventricular tumors via a computer-assisted volumetric stereotactic approach," *Neurosurgery*, 32, pp. 920-6, 1993.
3. Kelly P.J., Tumor stereotaxis New York: W. B. Saunders, 1991.
4. Nicholas Ayache, Philippe Cinquin, Isaac Cohen, Laurent Cohen, François Leitner, and Olivier Monga. Segmentation of complex three-dimensional medical objects: A challenge and a requirement for computer-assisted surgery planning and performance. In R. H. Taylor, S. Lavallée, G. C. Burdea, and R. Mäosges, editors, Computer-integrated surgery, Technology and clinical applications, chapter 4, pages 59-74. MIT Press, Cambridge Ma., 1995.
5. Ziv Yaniv and Kevin Cleary, "Image Guided Procedures: A Review" Technical Report CAIMR TR-2006-3,April 2006
6. P. J. Kelly, B. A. Kall, S. Goerss, and F. Earnest, "Computer-assisted stereotactic laser resection of intra-axial brain neoplasms," *Journal of Neurosurgery*, vol. 64, no. 3, pp. 427-439, 1986
7. Hastreiter P., Rezk-Salama C., Soza G., Bauer M., Greiner G., Fahlbusch R., Ganslandt O., Nimsky C. 2004, Strategies for brain shift evaluation. *Medical Image Analysis*, 8: 447–464
8. Nabavi, A., Black, P., Gering, D., Westin, C., Mehta, V., Pergolizzi, R., Ferrant, M., Warfield, S., Hata, N., Schwartz, R., Wells III, W., Kikinis, R., Jolesz F. 2001, Serial intra-operative magnetic resonance imaging of brain shift. *Neurosurgery* 48(4): 787–797.
9. P. J. Kelly, "Intraoperative brain shift and deformation: A quantitative analysis of cortical displacement in 28 cases - Comment," *Neurosurgery*, vol. 43, no. 4, pp. 759-759, Oct, 1998.
10. L. D. Lunsford, R. Parrish, and L. Albright, "Intraoperative imaging with a therapeutic computed tomographic scanner," *Neurosurgery*, vol. 15, no. 4, pp. 559-61, Oct, 1984.
11. H. Okudera, S. Kobayashi, K. Kyoshima, H. Gibo, T. Takemae, and K. Sugita, "Development of the operating computerized tomographic scanner system for neurosurgery," *Acta Neurochir (Wien)*, vol. 111, no. 1-2, pp. 61-3, 1991.
12. W. E. Butler, C. M. Piaggio, C. Constantinou, L. Nikalson, R. G. Gonzales, G. R. Cosgrove, and N. T. Zervas, "A mobile computed tomographic scanner with intraoperative and intensive care unit applications.," *Neurosurgery*, vol. 88, no. 4, pp. 1304-1310, 1998.
13. Kikinis, R., Gleason, W., Lorensen, W., Wells, W., Grimson W.E.L., Lozano-Perez, T., Ettinger, G., White, S., and Jolez, F. Image guidance techniques for neurosurgery. SPIE: Visualization in Biomedical Computing, pp. 537-540. 1994.
14. Hinks R.S., Bronskill M.J., Kucharczyk W., Bernstein M., and Collick R.M., "Magnetic Resonance Systems for Image Guided Therapy," *Journal of Magnetic Resonance Imaging*, 8 pp. 19-25, 1998.
15. P. M. Black, T. M. Moriarty, E. I. Alexander, P. Stieg, E. J. Woodard, P. L. Gleason, C. H. Martin, R. Kikinis, R. B. Schwartz, and F. A. Jolesz, "Development and Implementation of Intraoperative Magnetic Resonance Imaging and Its Neurosurgical Applications," *Neurosurgery*, vol. 41, no. 4, pp. 831-845, 1997.
16. R. Steinmeier et al. Intraoperative magnetic resonance imaging with the magnetom open scanner: Concepts, neurosurgical indications and procedures: A preliminary report. *Neurosurgery*, 43(4):739{748, 1998.

17. Moshe Hadani, Roberto Spiegelman, Zeev Feldman, Haim Berkenstadt, and Zvi Ram. Novel, compact, intraoperative magnetic resonance imaging-guided system for conventional neurosurgical operating rooms. *Neurosurgery*, 48(4):799-809.
18. J. W. Trobaugh, D. J. Trobaugh, and W. D. Richard, "Three-dimensional imaging with stereotactic ultrasonography," *Comput Med Imaging Graph*, vol. 18, no. 5, pp. 315-23, Sep-Oct, 1994.
19. R. M. Comeau, A. Fenster, and T. M. Peters, "Intraoperative US in interactive image-guided neurosurgery," *Radiographics*, vol. 18, no. 4, pp. 1019-27, Jul-Aug, 1998.
20. Gronningsaeter A, Kleven A, Ommedal S, Aarseth TE, Lie T, Lindseth F, Lango T, and Unsgard G, "SonoWand, an Ultrasound-based Neuronavigation System," *Neurosurgery* , 47, pp. 1373-1379, 2000.
21. Comeau R.M., Sadikot A.F., Fenster A., and Peters T.M., "Intraoperative ultrasound for guidance and tissue-shift correction in image-guided neurosurgery.", *Medical Physics* , 27, pp. 787-800, 2000.
22. Gobbi D.G., Lee B.L.K., and Peters T.M. Real-Time 3D Ultrasound for Intra-operative Surgical Guidance. *SPIE Medical Imaging MI01: Visualization, Display and Image-guided procedures, (This Volume)* 2001.
23. N. Archip, O. Clatz, S. Whalen, D. Kacher, A. Fedorov, A. Kot, N. Chrisocholdes, F. Jolesz, A. Golby, P. M. Black, and S. K. Warfield, "Non-rigid alignment of pre-operative MRI, fMRI, and DT-MRI with intra-operative MRI for enhanced visualization and navigation in image-guided neurosurgery," *Neuroimage*, vol. 35, no. 2, pp. 609-624, Apr, 2007.
24. N. Hata, T. Dohi, S. K. Warfield, W. M. Wells III, R. Kikinis, and F. A. Jolesz, "Multimodality Deformable Registration of Pre- and Intraoperative Images for MRI-guided Brain Surgery," *Proceedings of the First International Conference on Medical Image Computing and Computer-Assisted Intervention*, vol. 1496, no. 1998, pp. 1067-1074, 1998.
25. M. Bucki, C. Lobos, and Y. Payan, "Framework for a low-cost intra-operative image-guided neuronavigator including brain shift compensation," *Engineering in Medicine and Biology Society, 29th Annual International Conference of the IEEE*, vol. EBMS 2007, pp. 872-875, 2007.
26. H. Sun, D. W. Roberts, H. and Farid, Z. Wu, A. Hartov, and K. D. Paulsen, "Cortical Surface Tracking Using a Stereoscopic Operating Microscope," *Neurosurgery*, vol. 56, no. 1, pp. 86-97, 2005.
27. O. Skrinjar, A. Nabavi, and J. Duncan, "Model-driven brain shift compensation," *Medical Image Analysis*, vol. 6, no. 4, pp. 361-373, December, 2002.
28. S. K. Warfield, F. Talos, A. Tei, A. Bharatha, A. Nabavi, M. Ferrant, P. M. Black, F. A. Jolesz, and R. Kikinis, "Real-time registration of volumetric brain MRI by biomechanical simulation of deformation during image guided neurosurgery," *Computing and Visualization in Science*, vol. 5, no. 1, pp. 3-11, 2002
29. S. K. Kyriacou, A. Mohamed, K. Miller, and S. Neff, "Brain mechanics for neurosurgery: modeling issues," *Biomech Model Mechanobiol*, vol. 1, pp. 151-164, 2002.
30. K. K. Mendis, R. L. Stalnaker, and S. H. Advani, "A constitutive relationship for large deformation finite element modeling of brain tissue," *Journal of Biomechanical Engineering*, vol. 117, pp. 279-285, 1995
31. Marek Bucki, Olivier Palombi, Mathieu Bailet, Yohan Payan "Doppler Ultrasound Driven Biomechanical Model of the Brain for Intraoperative Brain-Shift Compensation: A Proof of Concept in Clinical Conditions" *Soft Tissue Biomechanical Modeling for Computer Assisted Surgery Springer-Verlag (Ed.) (2012) 135-165*

32. Reinertsen, I., Descoteaux, M., Siddiqi, K., Collins, D. "Validation of vessel-based registration for correction of brain shift. Medical Image Analysis" 11 (4), 374 – 388 (2007)
33. Sean Jy-Shyang Chen, Ingerid Reinertsen, Pierrick Coupè, Charles X. B. Yan, Laurence Mercier, D. Rolando Del Maestro, D. Louis Collins "Validation of a Hybrid Doppler Ultrasound Vessel-based Registration Algorithm for Neurosurgery" International Journal of Computer Assisted Radiology and Surgery 7, 5 (2012) 667-85
34. Payan Y., "Soft Tissue Biomechanical Modeling for Computer Assisted Surgery". Springer, Berlin ISBN 978-3-642-29013-8.
35. Marie-Ange Janvier, Louis-Gilles Durand, Marie-Helene Roy Cardinal, Isabelle Renaud, Boris Chayera, Pascal Bigrasc, Jacques de Guise, Gilles Soulez, Guy Cloutier, "Performance evaluation of a medical robotic 3D-ultrasound imaging system". Medical Image Analysis 12 (2008) 275–290.
36. Francois Conti1, Jaeheung Park, and Oussama Khatib, "Interface Design and Control Strategies for a Robot Assisted Ultrasonic Examination System"
37. Ta-Chih Lee and Rangasami L. Kashyap, " Building Skeleton Models via 3D Medial Surface/Axis Thinning Algorithms" CVGIP: Graphical Models and Image Processing Vol. 56, No. 6 November, pp. 462-478, 1994.
38. David A. Baderi and Joseph Jaja, "Parallel Algorithms for Image Histogramming and Connected Components with an Experimental Study" Journal of Parallel and Distributed Computing 35, 173–190 (1996) Article No. 0079
39. Aristeidis Sortiras, Christos Davatzikos, Nikos Paragios, "Deformable Medical Image Registration: A Survey", research report n°7919-Septemeber 2012
40. Barbara Zitova, Jan Flusser, "Image registration methods: a survey" Image and Vision Computing 21 (2003) 977–1000
41. John W. Norris, Alison Halliday, "Is Ultrasound Sufficient for Vascular Imaging Prior to Carotid Endarterectomy?" Advances in Stroke 2003
42. Gail ter Haar, "Ultrasonic imaging: safety considerations" Recent advances in biomedical ultrasonic imaging techniques.
43. Diagnostic Ultrasound Safety A summary of the technical report "Exposure Criteria for Medical Diagnostic Ultrasound: II. Criteria Based on all Known Mechanisms" issued by the National Council on Radiation Protection and Measurements, United States.
44. Peter N Burns, "Introduction to the Physical Principal of Ultrasound Imaging and Doppler" MBP1007/1008, Fundamentals in Medical Biophysics, Sunnybrook Health Science Centre.
45. William Goh, Ivica Zalud, "To Doppler or Not to Doppler: From Doppler Ultrasound to Color Doppler to Doppler in 3D and Beyond" Donald School Journal of Ultrasound in Obstetrics and Gynecology, April-June 2011;5(2):159-166
46. W. N. McDicken and T. Anderson, "The Difference Between Colour Doppler Velocity Imaging and Power Doppler Imaging" *Eur J Echocardiography* (2002) 3, 240–244
47. Barry CD, Allott CP, John NW, Mellor PM, Arundel PA, Thomson DS, Waterton JC., Three-dimensional freehand ultrasound: image reconstruction and volume analysis. *Ultrasound Med Biol.* 1997; 23(8):1209-24.
48. Jun S. Haa John A. Hossacka and Thilaka S. Sumanaweera. "Quantitative, free-hand 3dultrasound imaging based on a modified 1d transducer array." *Biomedical Engineering, University of Virginia*
49. Philippe Thévenaz, "Interpolation Revisited" *IEEE Transactions on Medical Imaging*, vol. 19, no. 7, July 2000

50. Jin Li and Andrew D. Heap, "A Review of Spatial Interpolation Methods for Environmental Scientists" Record 2008/23
51. Philippe Thévenaz, Thierry Blu and Michael Unser, "Image Interpolation and Resampling" Handbook of medical imaging, Pages 393-420, Academic Press, Inc. Orlando, FL, USA, 2000
52. Reinertsen I, Collins DL., "A realistic phantom for brain-shift simulations." Med Phys. 2006 Sep;33(9):3234-40.
53. Bucki M., Lobos C. & Payan Y., "A Fast and Robust Patient Specific Finite Element Mesh Registration Technique: Application to 60 Clinical Cases." Medical Image Analysis, Vol. 14, pp. 303–317.
54. Harry Blum, "A Transformation for Extracting New Descriptors for Shapes"
55. Cornea N. D. "Curve-skeletons: properties, computation and applications", PhD thesis, Rutgers, The State University of New Jersey, 2007.
56. T.C. Lee, R.L. Kashyap, and C.N. Chu, "Building skeleton models via 3-D medial surface/axis thinning algorithms." Computer Vision, Graphics, and Image Processing, 56(6):462–478, 1994.
57. G. Malandain, G. Bertrand, and N. Ayache, "Topological segmentation of discrete surfaces" International Journal of Computer Vision, 10(2):183-197, 1993
58. Hanno Homann, "Implementation of a 3D thinning algorithm" The Insight Journal - 2007 July - December.
59. Derek L.G. Hill, Philipp G. Batchelor, Mark Holden, and David J Hawkes, "Medical image registration" Phys. Med. Biol. 46 (2001) R1–R45
60. Aristeidis Sotiras, Christos Davatzikos, Nikos Paragios, "Deformable Medical Image Registration: A Survey"
61. Saito T., Toriwaki, J., 1994. 'New algorithms for euclidean distance transformations of an n-dimensional digitized picture with applications' Pattern Recognition 27, 1551–1565
62. Stina Svensson and Gabriella Sanniti di Baja, "Simplifying curve skeletons in volume images", Computer Vision and Image Understanding 90 (2003) 242–257
63. D. Shaked, A.M. Bruckstein, "Pruning medial axes", Computer Vision Image Understanding 69 (2) (1998) 156–169.
64. I. Nystrom, "Skeletonization applied to magnetic resonance angiography images", in: K.M. Hanson (Ed.), Medical Imaging 1998: Image Processing, Proc. SPIE 3338, 1998.
65. Ralph J.M. Peter, Henk A. Marquering, Halil Doğan, Emile A. Hendriks, Albert de Roos, Johan H.C. Reiber, Berend C. Stoel, "Labeling the Pulmonary Arterial Tree in CT Images for Automatic Quantification of Pulmonary Embolism", Proceedings of SPIE - Volume 6514 - Medical Imaging -Computer-Aided Diagnosis, San Diego, no. 6514, February 2007.
66. W.H. Tang and Albert, C.S. Chung, "Cerebral Vascular Tree Matching of 3D-RA Data Based on Tree Edit Distance", Medical Imaging and Augmented Reality Lecture Notes in Computer Science Volume 4091, 2006, pp 116-123
67. D. Attali, A. Montanvert, "Computing and simplifying 2D and 3D continuous skeletons", Computer Vision Image Understanding 67 (3) (1997) 261–273
68. Wachinger C, Wein W, Navab N, "Three-dimensional ultrasound mosaicing." Med Image Comput Comput Assist Interv. 2007; 10(Pt 2):327-35.
69. Muhammad Adil Hayat Khan, "3D Reconstruction of Ultrasound Images", MSc Vision and Robotics. 2008

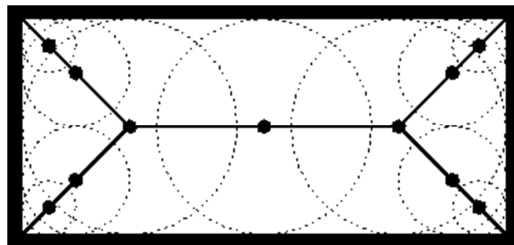
Appendix A

A.1 Medial Axis/Curve Skeleton

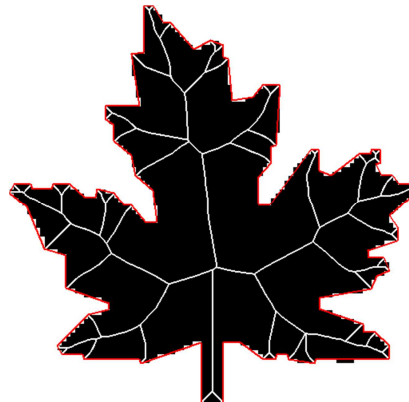
In shape analysis, **skeleton** (or **topological skeleton**) of a shape is a thin version of that shape that is equidistant to its boundaries. The skeleton usually emphasizes geometrical and topological properties of the shape, such as its connectivity, topology, length, direction, and width. Together with the distance of its points to the shape boundary, the skeleton can also serve as a representation of the shape (they contain all the information necessary to reconstruct the shape).

A formal definition: the skeleton is the locus of the centers of all maximal inscribed hyper-spheres (i.e., discs and balls in 2D and 3D, respectively). (An inscribed hyper-sphere is maximal if it is not covered by any other inscribed hyper-sphere.)

Another definition: skeleton is the loci of centers of bi-tangent circles that fit entirely within the foreground region being considered.



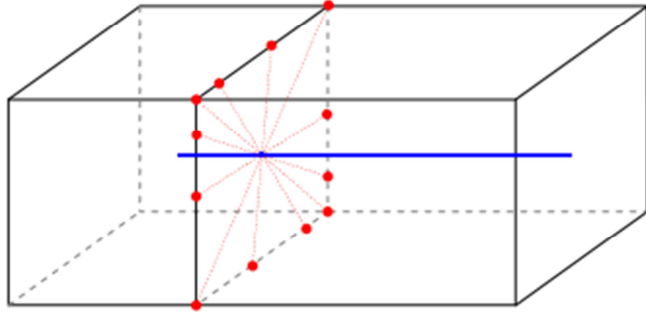
Skeleton of a Rectangle defined by loci of bi-tangent circles



Skeleton with Noise

A.2 Centeredness of the Curve Skeleton

Curve-skeletons are composed of curve segments. Curve-skeleton segment is centered within the object, if every point on the curve segments is centered within the object in a plane normal to the curve segment at that point.



Centeredness of a Curve Skeleton

Given a curve skeleton in a digital 3D image, it is important to measure the centeredness at path points to evaluate the centeredness of the curve skeleton.

Given a curve point the tangent is measured using median differencing [68] the corresponding normal plane is derived. Rays are shot along the plane and the distance to the object boundary is measured and averaged to find the radius predicted by the curve skeleton. This value averaged over the curve skeleton can be used to measure the centeredness of the curve skeleton given the actual radius of the object is a prior knowledge.